Vrije Universiteit Brussel

Faculteit Ingenieurswetenschappen
Dienst Stromingsmechanica

CFD Simulatie van Stroming in Realistische Longgeometrieën

Proefschrift ingediend met het oog op het behalen
van de graad van Master in de Ingenieurswetenschappen

Kasper De Geeter

Promotor: Prof. Dr. Ir. Chris Lacor
Begeleiders: Ir. Vivek Agnihotri

MEI 2010

Vrije Universiteit Brussel

Faculty of Applied Sciences & Engineering
Department of Fluid Mechanics

CFD Simulation of Flow in Realistic Lung Geometries

Graduation thesis submitted in partial fulfillment of the
requirements for the degree of Master in the Engineering Sciences

Kasper De Geeter

Promotor: Prof. Dr. Ir. Chris Lacor
Advisors: Ir. Vivek Agnihotri

MAY 2010

ABSTRACT

Computational fluid dynamics (CFD) is a novel tool in the medical world. Much research is devoted to phenomenona occurring in flow, be it blood or air, in a way that has not been done before. This provides new insights in medicine, and might improve existing medical practice.
This thesis looks at the flow of air in realistic lung geometries, using Fluent, a commercially available CFD package.

We look at different options to model the flow using a realistic geometries based on CT-scans, provided to us by the university of Antwerp. These geometries feature asymmetry, threedimensional bifurcations and non-smooth surfaces that are not always accounted for in simplified geometries. However, problems may arise because of the limited resolution of the CT-scan.
We also look at the effect of the resection of a lobe.

We simulated the flow field varying the different options we have (boundary conditions, turbulence models, solver settings, ...). We simulated the effect of the lobectomy using the settings found for the full geometry.

We found that using the SST $k-\omega$ turbulence model and pressure outlets we obtain the best (most realistic) results.

SAMENVATTING

Computational Fluid Dynamics is een nieuwe tool in de medische wereld. Hedentendage wordt er veel onderzoek gedaan naar de stroming van lichaamsvocht, zij het bloed of lucht, op een manier die tevoren niet mogelijk was. Deze nieuwe technieken zorgen voor nieuwe inzichten in de geneeskunde en kunnen mogelijk leiden tot meer efficiënte, therapieën.
In deze thesis wordt de stroming van de lucht in realistische longgeometrieën bestudeerd, en de problemen die daarbij optreden, gebruikmakend van Fluent, een commercieel CFD pakket.

We kijken naar de verschillende mogelijkheden die bestaan om de stroming te modelleren. We gebruiken realistische longmodellen, gebaseerd op CT-scans, die werden aangeleverd door de Antwerpse universiteit. Deze realistische geometrieén vertonen asymmetrie, driedimensionele bifurcaties en oneffenheden. Deze zijn niet altijd aanwezig in vereenvoudigde modellen. Hoewel deze model meer realisme brengen, brengen ze ook problemen met zich mee, mede tengevolge van de beperkte resolutie van de CT-scan.
We bekijken ook het effect van een lobectomie op de rest van de long.

We simuleren het fluidum door al de opties (boundary conditions, turbulentiemodel, instellingen van de solver, ...) te laten variëren. De stroming in de long met een verwijderde kwab, simuleren we gebruikmakend van de eerder gevonden instellingen.
We concluderen dat het SST $k - \omega$ turbulentiemodel samen met een vaste

druk aan de uitlaten de meest realistische oplossingen levert.

RÉSUMÉ

Computational Fluid Dynamics (CFD) est un outil nouveau dans le monde médical. Beaucoup de recherche est consacrée à l'étude des phénomènes qui se produisent dans les flux biologiques, que ce soit de sang ou d'air, d'une manière qui n'a pas été possible avant. Cette recherche offre de nouvelles perspectives en médecine, et pourrait aborder à une amélioration de la pratique médicale actuelle. Cette mémoire porte sur le flux d'air dans des géométries réalistes du poumon. Elle a été effectuée à l'aide d'un programme commercial de CFD, sous le nom de Fluent. Elle a également étudié les problèmes qui peuvent se produire en utilisant le programme.

Nous avons examiné les différentes options à notre disposition pour modéliser le flux dans des géométries réalistes basées sur le scanner CT, qui nous ont été fournis par l'université d'Anvers. Cette géométrie présente des asymmétries, des bifurcations en trois dimensions et des surfaces non lisses qui ne sont pas toujours représentés dans les géométries simplifiées. Bien que ces géometries sont plus proches de la réalité, elles peuvent emporter des problèmes en raison de la résolution limitée du CT-scan.
Nous avons également examiné l'effet de la resection d'un lobe.

Nous avons simulé le champ d'écoulement en utilisant une variation des différentes options (les conditions aux limites, le modèle de turbulence, les paramètres du solveur, ...). Nous avons utilisé les paramètres trouvés pour la géométrie pleine pour la simulation de l'effet du lobe réséqué.

Nous avons constaté que les meilleures solutions, c'est à dire les solutions les plus réalistes, sont obtenues à l'aide du modèle de turbulence SST $k - \omega$ et des pressions fixes au niveau des sorties.

ACKNOWLEDGMENTS

Firstly I would like to thank professor Lacor, for giving me the opportunity to work on a subject, different from hot water (which I invented), that captures my imagination.
I would also like to thank Vivek for his ceaseless effort to try and enlighten me. Without the time he devoted to me and my thesis, this would still be a blank page.

I would also like to thank my parents, for feeding me and providing me with the opportunity to enjoy all the fun that comes with studying in August. My brother deserves a mention for keeping my reflexes strong, my laughing muscles well trained, and having a computer.
My girlfriend, Anne-Sophie, should also be mentioned, for cleaning my room and providing me with love, care and support.

Special thanks (to the extreme) should go to my friends and colleagues of the LURU, for providing me with a wall full of waste of time and general entertainment.

A honorary mention should go to my bike, which I inherited from my great grandfather, and which got stolen while I was writing this thesis at the department of fluid mechanics.

CONTENTS

LIST OF FIGURES

LIST OF TABLES

NOMENCLATURE

CFD	Computational Fluid Dynamics
COPD	Chronic Obstructive Pulmonary Disease
DES	Detached Eddy Simulation
ERV	Expiration Reserve Volume
FEV1	Forced Expiratory Ventilation in one second
FRC	Functional Residual Capacity
GCI	Grid Convergence Index
HRCT	High Resolution Computed Tomography
IRV	Inspiratory Reserve Volume
LBM	Lattice-Boltzmann Method
LES	Large Eddy Simulation
LLL	Left Lower Lobe
LUL	Left Upper Lobe
RANS	Reynolds Averaged Navier-Stokes
RLL	Right Lower Lobe

RML	Right Middle Lobe
RSM	Reynolds Stress Model
RUL	Right Upper Lung
RV	Reserve Volume
SPECT	Single Photon Emission Computed Tomography
TLC	Total lung capacity
TV	Tidal Volume
VC	Vital Capacity

CHAPTER

ONE

INTRODUCTION

Computational fluid dynamics (CFD) is a tool that is increasingly used in medical applications [6, 9, 7, 8, 24, 3, 25, 27, 16] and may provide valuable information for clinical practice, possibly giving lead to better treatments or detection methods. However, some problems still stand in the way of CFD as a regular tool for physisicians.

CFD calculations must produce results that are a close approximation of reality. However, there are many parameters that can be set, and not all combinations of parameters produce results that match reality closely. Calculations should also be possible within a reasonable timespan, to make clinical use possible. This includes model generation (CT or MRI scan + mesh generation), the time necessary to reach a converged solution and the time necessary to postprocess results.

This thesis is part of three studies comparing different solvers, namely Fluent (Ansys), Fine/Hexa (Numeca) and COOLFluid (von Karman Institute). The research question is which solver produces the best solution, and has the greatest ease of use. This is the part about the Fluent solver.

This thesis starts with a literature survey. The next chapter provides the reader with some knowledge about the medical side of the story. In chapter four the optimal settings are determined and in chapter five the results obtained using these settings are discussed, both for the full lung and for the resected geometry.

CHAPTER

TWO

LITERATURE SURVEY

Many studies have been performed on simplified airway geometries such as the Weibel [26] model, which describes the bronchi as a symmetric tree structure of bifurcating tubes with 23 generations. These studies have provided valuable information about internal flow and particular characteristics of respiratory flow such as secondary flow and inertial effects. These models however did not take into account morphological variations from generalized geometries that exist in the human population. Such variations are even more pronounced in diseased patients. The effect of three-dimensional bifurcations, non smooth surfaces, and the impact of asymmetric branching have not always been incorporated in simplified models.

Nowak et al. [21] compared two geometries, one based on the Weibel A model, the other based on a CT scan of a cadaver lung cast. Unsteady and steady calculations were compared. These authors concluded that there is no consistent

pattern of similarity between the simplified model and the realistic model. They also stated that differences between steady and unsteady solutions make the former unreliable for particle deposition.

Brouns et al. [3] studied tracheal stenosis (narrowing of the trachea) using computational fluid dynamics (CFD). Patients having tracheal stenosis usually do not exhibit any symptoms until critical narrowing of the trachea occurs. Brouns et al. tried to develop a method to predict tracheal stenosis before it is critical. It was observed that a dramatic pressure drop only occurred when well over 70% of the trachea was obstructed. A hexahedral mesh containing about 650000 cells was used on a realistic smoothed upper airway model. A rule of thumb was derived from which pressure drops over the stenosis can be estimated on the basis of breathing flow and stenosis cross section. In addition, CFD simulations suggested that the best-fit exponent in the power law that relates upper airway resistance to volumetric flow could indeed be used as a diagnostic tool in the noninvasive monitoring of stenosis patients.

Jayaraju et al. [14] studied a CT based realistic upper airway model. In contrast to most idealized mouth-throat models, they reported a transition at a flow rate of 15 l/min. Kinetic energy levels increased after the glottis indicating the sensitivity to geometrical complexities at low flow rates.

The influence of the glottic aperture was studied by Brouns et al. [4]. The extra-thoracic region has a major influence on the aerosol delivery to the

proximal or peripheral intra-thoracic airways. In order to characterize the particle deposition in this area, it is important to first investigate the flow structures in this region. The glottis, which is delimited by the vocal cords and therefore has the narrowest passage, generates a laryngeal jet resulting in complex secundary structures downstream of the glottis. It is generally assumed that the glottis has different shapes and cross-sectional areas at different moments during the respiratory cycle and also depends on the average inspiratory flow rate. Therefore, the influence of a circular glottal aperture, with a cross-sectional area of 90mm^2 and an elliptical and triangular shape, both with an area of 45mm^2, on the flow was investigated. The circular glottal aperture had almost no influence on the flow structure. The triangular aperture on the other hand, shifted the laryngeal jet to the posterior side, generating two pairs of counter rotating vortices. The difference in pressure drop was more dominated by the cross-sectional area than by the shape of the glottis. It was also reported that the flow structures did not change significantly between different flow rates.

In the thesis of Brouns [2] a comparative study was done of different turbulence models, namely SST $k-\omega$, realizable $k-\epsilon$ and the Reynolds Stress Model. The general flow fields that were found using these models all looked about the same, but differed in details. Velocity profiles in the trachea were best predicted by the low Reynolds number SST $k-\omega$ turbulence model. However, the velocity profile of the pharyngeal jet differed from the measured profile. For higher flow rates the turbulent kinetic energy was quite well predicted, but for lower rates the turbulence model(s) overestimated the

turbulence kinetic energy, which is a problem for particle deposition studies. Brouns concluded that SST $k-\omega$ is a viable alternative to the computationally more expensive detached eddy simulation and large eddy simulation turbulence models.

Longest and Vinchurkar [18] have studied the effect of different mesh styles on the flow field in an attempt to better understand the effects of the mesh on the velocity fields and deposition patterns in bifurcating respiratory models. Generating structured meshes based on hexahedral elements requires significant time and effort but these meshes often lead to high quality solutions. Unstructured meshes that use tetrahedral elements can be constructed much faster but may increase levels of numerical diffusion, especially in tubular flow systems with a primary flow direction. Four widely used mesh styles including structured hexahedral, unstructured tetrahedral, flow adaptive tetrahedral, and hybrid grids have been considered for two respiratory airway configurations. Accuracy of the simulations has been assessed by comparisons with experimental in vitro data available. Quantitative grid convergence was assessed based on a grid convergence index (GCI), which accounts for the degree of grid refinement. The hexahedral mesh was observed to have GCI values that were an order of magnitude below the unstructured tetrahedral mesh values for all resolutions considered. Moreover, the hexahedral mesh style provided GCI values of approximately 1% and reduced run times by a factor of 3. The mesh style was found to have an observable effect on the total particle depositions with the hexahedral solution most closely matching empirical results. However Longest and Vinchurkar conclude that all other

mesh styles still produce solutions that are in reasonable agreement with experiments.

Luo and Liu [19] investigated the inspiratory flow characteristics in a CT-scan based lung model using a low Reynolds number $k-\omega$ turbulence model. They used pressure outlets that were set uniformly. They reported differences in flow patterns between laminar and turbulent flow. The secondary flow was stronger in the laminar case than in the turbulent case.

Jayaraju et al. [15] simulated flow in a human mouth-throat model under normal breathing conditions using Reynolds averaged Navier-Stokes (RANS) $k-\omega$, DES and LES methods. They validated their results using PIV measurements on an identical model cast. Velocity and kinetic energy profiles obtained with DES and LES simulations showed better agreement with the experiment than did the $k-\omega$ model. Considerable differences were found in particle deposition between DES/LES and $k-\omega$. In conclusion Jayaraju et al. stated that DES/LES provide more accurate results than the RANS $k-\omega$ model. It should be noted that for particle tracking purposes DES/LES perform equally wel for particles bigger than 5μm.

In De Backer et al. [8] the need for patient-specific geometries and boundary conditions was explored. To this end two CT-scans were made, one at total lung capacity (TLC) and one at functional residual capacity (FRC) . The model itself was then derived from the CT images using commercial software (Micmics 10.0, Materialise, Belgium). By taking scans at two different levels it

is possible to obtain an estimate of the relative lung expansion, which, with the boundary conditions in mind, is valuable information. A high quality, unstructured, tetrahedral mesh was made using the commercial software TGrid. Meshes were made with $1.5 \cdot 10^6$, $3 \cdot 10^6$ and $4.5 \cdot 10^6$ cells. Very little difference in mass flow distribution were observed. These authors also studied two cases employing different boundary conditions. In the first case the pressure at all outlets was set uniformly. In the second case the pressures at the left and right lung were varied in order to get the correct mass distribution. De Backer et al. [8] concluded that the results attained using patient-specific boundary conditions corresponded better with the in vivo test.

Freitas and Schrder [10] used a model based on a cast of a human lung down to the 6^{th} generation. They used a lattice-Boltzmann method (LBM) , which has been shown to solve the Navier-Stokes equations. The LBM is a special solution algorithm to solve isothermal, incompressible and low Reynolds continuum flow. It is based on the Boltzmann equation. There are some advantages to the use of the LBM. It efficiently describes multi-phase flows, has a low computational cost, very good parallel scale-up capabilities, and a very efficient treatment of fixed wall boundary conditions. It has some drawbacks but they are no danger to the case at hands. The authors found their results to be in very good agreement with PIV measurements. Freitas and Schrder reported a turnover time (from meshing to steady-state solution) of less than 12 hours.

De Backer et al. [7] used CFD to detect changes in airway resistance in asth-

matics after acute bronchodilation. The study was performed on 14 patients. With a standard examination (Forced Expiratory Ventilation in one second (FEV1) , Vital Capacity (VC)) it is difficult to assess changes in local resistance, as these parameters only provide global information. Patient specific models were obtained using a high resolution computed tomography (HRCT) scan. The smallest bifurcations modelled had a diameter of about 1-2 mm. This corresponds to bifurcations of the 5^{th}-7^{th} generation. De Backer et al. modelled the flow using an incompressible, isothermal and laminar flow. The laminar flow was chosen because of the limited influence of turbulence on the regions where the highest resistance is present (4^{th}-7^{th} bifurcation). The pressure at the outlets was set uniformly. Because of variation between different patients these pressures vary between -1000 Pa and -1500 Pa. These values are rather high, as the patients considered are asthmatic. Unstructured tetrahedral meshes were used. Typical mesh size was about $3 \cdot 10^6$ cells. The computed change in total resistance of the airway was found to correlate with the results from the spirometry test.

Gemci et al. [11] based their CFD analysis on the geometry by Schmidt et al. [23]. The model is derived from a CT-scan but has been processed to develop an abstract graph representation. Specially adapted image processing algorithms were applied to segment and delineate the bronchi. The graph thus obtained contains topological information about spatial coordinates, connectivities, diameters and branching angles. Seventeen airway generations have been modelled. The mouth and glottis were not included in this model because they were thought to have little effect on the total resistance of the

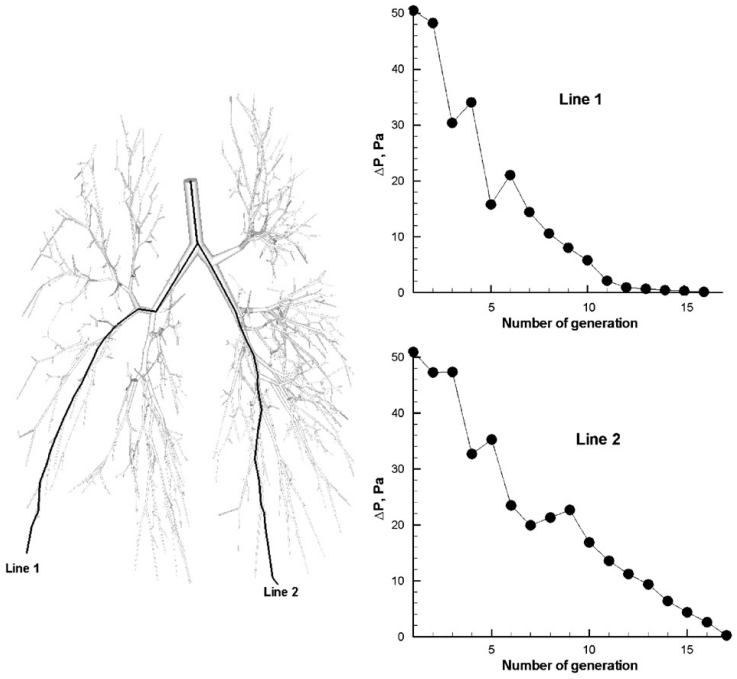

Figure 2.1: Pressure drop along two selected paths [11].

lung. The mesh used by Gemci et al. contained $6.7 \cdot 10^7$ unstructured tetrahedral cells. They used LES. A mass flow inlet and outflow boundary condition were used. A static pressure drop of 50 Pa was reported by Gemci et al. at a volumetric flow rate of 28.3 l/min.

CHAPTER

THREE

THE RESPIRATORY SYSTEM

3.1 Pulmonary System

The pulmonary system delivers oxygen to the bloodstream and removes (mainly) carbon dioxide from the blood. The lungs are located in the chest at both sides of the heart.

3.1.1 Physiology

While a person breathes in, the human pulmonary system leads the air, via the nasal or oral cavity through respectively the nasopharynx or oropharynx into the larynx. The air is then conducted through the trachea, which bifurcates to form the main bronchi, which lead to the left and right lung. The main bronchi then divide into bronchi, bronchioles and terminal bronchioles. At this point the air has passed the conducting zone. The airway divides even

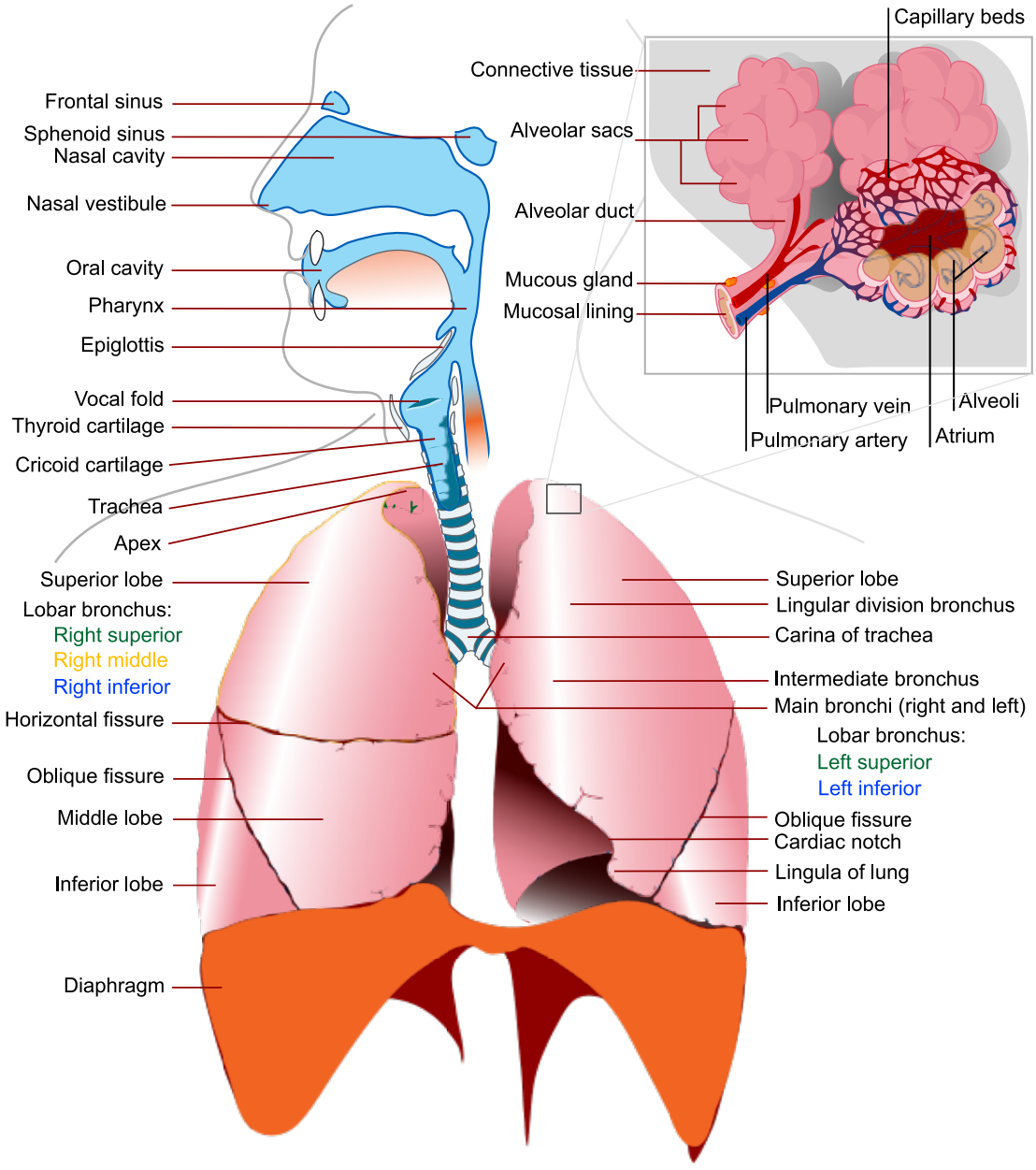

Figure 3.1: The pulmonary system. [22]

further to form the transitional and respiratory zone. The branches in this zone are called, in order of their appearance in the respiratory tract, alveolar ducts and alveolar sacs. The airway divides a total of 23 times between trachea and alveoli. The first 16 divisions are part of the conduction zone, the last 7 are part of the respiratory zone. Because of all these divisions the total cross section of the lung is largely increased. The total wetted area of a human lung is about 70 m^2 and is covered by about 300 million alveoli. These alveoli are surrounded by pulmonary capillaries that deliver blood to the lung.
The lung is divided into lobes. The right lung has 3 lobes, the right upper lobe, the right middle lobe and the right lower lobe (RUL, RML, RLL) . The left lung has 2 lobes, the left upper lobe and the left lower lobe (LUL, LLL). The lungs are separated from the chest by the pleural cavity. [13]

3.1.2 Breathing Mechanics

A normal person at rest takes about 12 to 15 breaths per minute. Each breath has a volume of about 500 ml.
Two phases can be discerned: inspiration and expiration.

Inspiration

Inspiration is an active process, meaning that muscle activity is necessary to do it. While a person breathes in, a contraction of the inspiratory muscles decreases the intrapleural pressure, which is slightly negative at rest (-2.5 mmHg), to -6 mmHg. This causes the lung to expand, thus lowering the pressure in the lungs, making it lower than the atmospheric pressure and

allowing air to flow into the lungs.

Expiration

Expiration is a passive process in rest. The recoil pressures of the lung and the chest wall balance and the relative pressure in the lung becomes slightly positive, allowing the air to flow out. In heavy breathing, the extent of lung deflation is increased by active contraction of the expiratory muscles. The intrapleural pressure can drop as low as -30 mm Hg.

3.2 Measurement Techniques

Classical techniques to assess lung function are described below.

3.2.1 Spirometry

Spirometry is the most common of the pulmonary test. It measures the volume of exhaled air and the speed at which this happens. It can be used to evaluate COPD (Chronic Obstructive Pulmonary Disease) , asthma, etc.
The amount of air that moves in and out of the lung in every inspiration/expiration cycle is called the tidal volume (TV) . Air inspired with maximal effort in excess of the tidal volume is called the inspiratory reserve volume (IRV). When exhaling actively the expiration reserve volume (ERV) is exhaled. Then only the reserve volume (RV) is left in the lung.
The vital capacity is defined as the largest amount that one can expire after a maximal inspiratory effort. The fraction of the vital capacity that is exhaled

	Man (l)	Woman (l)
IRV	3.3	1.9
TV	0.5	0.5
ERV	1	0.7
RV	1.2	1.1
Total Volume	6	4.2

Table 3.1: Average lung volume.

in the first second is called the FEV1. In some cases the vital capacity can be normal but the FEV1 is reduced. For example, this is observed in asthma patients, because of a larger airway resistance.

The maximum voluntary ventilation is the largest amount of gas that can be moved in and out of the lung in one minute. Typical values are 125 to 170 l.

3.2.2 Scintigraphy

Radionuclide imaging techniques allow to evaluate physiology and function, as distinguished from organ anatomy. The principles are largely unchanged since the sixties.

The most common indication for Ventilation/Perfusion scintigraphy is the evaluation of suspected pulmonary embolism.

Perfusion Scintigraphy

The principle of perfusion scintigraphy is simple. If a large number of radiolabeled particles, too large to pass through the pulmonary bed, are injected in the bloodstream near the lungs, they will be trapped in the pulmonary vas-

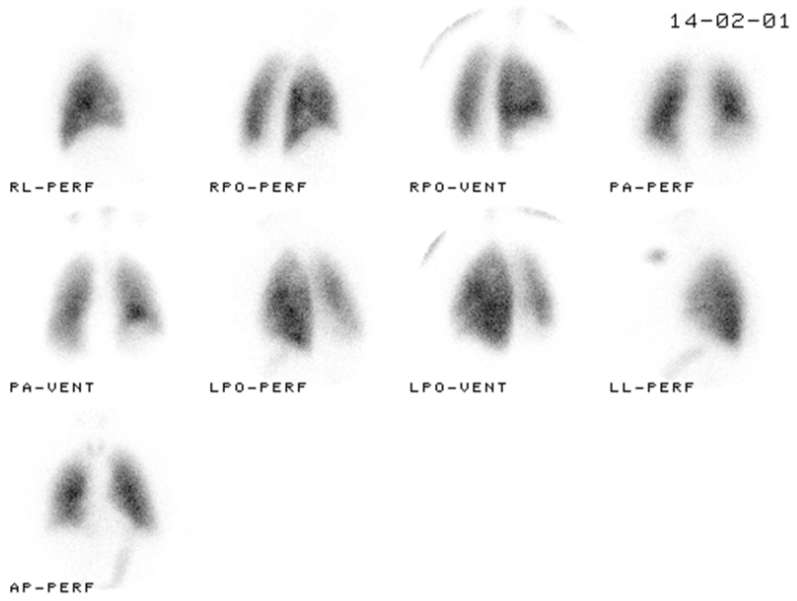

Figure 3.2: Typical image of a V/P scintigraphy.

cular bed. Their distribution will be proportional to the regional pulmonary blood flow. Once these particles have set, they can be seen using conventional nuclear medicine gamma scintillation cameras. These images provide a map of regional pulmonary perfusion. Well perfused areas will demonstrate uniform activity (uniform dark regions) and areas of decreased or absent perfusion will appear as areas with lower count density. Multiple projections are used.

A standard pulmonary perfusion study consist of planar images, anterior, posterior, 45-degrees right and left posterior obliques, 45-degrees right and left anterior obliques, and left and right lateral views. The posterior images are of highest importance, since they best demonstrate the lower lobes (the most common site of pulmonary embolism).

Planar images may be supplemented by SPECT (Single Photon Emission Computed Tomography) to better identify and localize perfusion defects.

Ventilation Scintigraphy

In everyday medical practice ventilation of the lower airways is assessed using ventilation scintigraphy. This is usually performed in conjunction with perfusion scintigraphy in the evaluation of pulmonary embolism. During this test the patient either inhales an inert radioactive gas or a fine submicronic aerosol at tidal breathing levels. The particles in such an aerosol have very small Stokes numbers.

$$Stk = \frac{V\rho_p D_p^2}{18\mu L} \tag{3.1}$$

with V the stream velocity, ρ_p the particle density, D_p the particle diameter, μ the dynamic viscosity and L a characteristic length. [5]

Particles with very small Stokes numbers follow the streamlines closely. This makes sedimentation the primary deposition mechanism. The distribution of the particles is traced using a gamma camera. The resulting image is used to assess local lung ventilation.

A ventilation study with ^{133}Xe consists of three phases: single breath inhalation, equilibrium wash-in and equilibrium wash-out. The study is conducted

with a spirometric apparatus similar to that used in pulmonary function testing. The patient gets an airtight mask and gets administered a quantity of ^{133}Xe as he/she inhales. The patient is then instructed to hold his/her breath while the image is being made. The distribution of radioactive material in the lung reflects regional pulmonary ventilation, with well ventilated regions showing uniform activity and poorly ventilated areas showing decreased or absent activity.

Following the single breath image, the patient breaths a mixture of oxygen and xenon for several minutes. Sometimes a series of posterior wash-in images are taken during this period, which lasts 3 to 5 minutes. Alternatively a single wash-in image is taken at the end of this period. This image may demonstrate the filling in of defects seen on the single breath image. The activity on the equilibrium wash-in image thus reflects overall ventilated lung volume.

During the final phase the patient breathes normal room air in and exhales the xenon gas. During this stage images are taken at 30s interval, for at least 5 minutes. In healthy individuals the wash-out is complete in about 3 minutes. Areas of slow wash-out indicate the presence of acute or chronic obstructive airway disease. If possible 45-degree right and left posterior images are taken to better localize defects. The wash-out phase is the most sensitive for the detection of obstructive airways disease.

In Europe, gas ventilation studies more frequently use ^{81m}Kr, because of its

favorable physical characteristics, including a short radioactive halflive of 13 s. This gas is also administered through a face mask but the patient continues to breathe it during image acquisition. Tomographic imaging is a possibility. The images reflect regional ventilation as such.

Definitions	
Forced Expiratory Volume in 1s (FEV1)	The amount of air exhaled during a forced expiratory manoeuvre in one second. This value represents the patient's ability to move air out of the lungs and reflects expiratory airway mechanics
Total Lung Capacity (TLC)	The lung volume attained after deep inhalation
Functional Residual Capacity (FRC)	The lung volume attained after normal expiration
Tidal Volume (TV)	The volume of air that moves in and out of the lung during normal breathing
Inspiratory Reserve (IRV)	The volume of air inhaled with maximal effort in excess of the tidal volume
Vital Capacity (VC)	The volume change of the lung between a full inspiration and a maximal expiration
Residual Volume (RV)	The volume of the lung after maximal exhalation started from the functional residual capacity.

Table 3.2: An overview of often used terms and their abbreviation.

CHAPTER

FOUR

MODEL

In this chapter all the necessary parameters are studied in order to obtain a stable, physically correct, solution. This starts with choosing the correct models, and continues with the choice of correct boundary conditions. The solver settings are also briefly mentioned in this chapter.

4.1 Navier-Stokes Equations

The Navier Stokes equations in their most general form are written as [17]:

$$\rho_{,t} + (\rho v_k)_{,k} = 0 \tag{4.1}$$

$$(\rho v_k)_{,t} + (\rho v_k v_l)_{,l} = -p_{,k} + \tau_{kl,l} \tag{4.2}$$

$$(\rho E)_{,t} + (\rho H v_k)_{,k} = (\tau_{lk} - q_k)_{,k} \tag{4.3}$$

with ρ the density, v the velocity, p the pressure, E the total energy per unit mass, H the total enthalpy per unit mass, τ the shear stress tensor and q the heat flux.

No analytical solution exist for these equations. We can however solve these equations using a computer. When we discretize the unchanged equations we have a Direct Numerical Simulation (DNS). Since these equations also model turbulence, which appears in a range of scales from very large to very small, we would need a very fine mesh to capture the entire range of turbulence scales. This makes DNS impossible to use in almost all practical cases because of the high computational cost that comes with very fine meshes.

Large Eddy Simulations (LES) use a different approach. The Navier Stokes equations are filtered by averaging in space. This filters out the smallest turbulence scales and retains the larger scales. Now the small turbulence scales have to be modelled. This allows to calculate on coarser grids than necessary for DNS and therefore has a lower computational cost.

The most commonly used form of the Navier-Stokes equations are the Reynolds Averaged Navier-Stokes equations (RANS). In this approach all turbulence is removed by averaging in time, and has to be replaced by modelling. Several turbulence models have been developed to do this.

RANS modelling is the obvious choice for this thesis, as LES is very time consuming and limited resources are available.

4.1.1 Turbulence Modelling

The choice of a turbulence model is not straightforward. It depends on several factors such as:

- the physics of the simulated flow
- the available computational resources
- established practice for a specific class of simulations
- the level of accuracy required

A whole range of turbulence models exist. The models implemented in Fluent are the one equation Spalart-Allmaras model, several $k-\epsilon$ models, different $k-\omega$ models and the Reynolds stress model (RSM).

The SST $k-\omega$ model was developed by Menter [20] to blend the robust and accurate formulation of the $k-\omega$ model in the near wall region with the free-stream independence of the $k-\epsilon$ model in the far field. To blend these models the standard $k-\epsilon$ model has been transformed into equations containing k and ω. The SST $k-\omega$ is similar to the standard $k-\omega$ model, but includes refinements:

- The standard $k-\omega$ and the transformed $k-\epsilon$ model are multiplied with a blending function that activates the standard $k-\omega$ and disables the transformed $k-\epsilon$ model in the near-wall region and the other way around in the free stream;

- The SST model has a damped cross-diffusion derivative term in the ω equation;

- The definition of turbulent viscosity is modified to account for the transport of the turbulent shear stress;

- The modelling constants are different.

All these changes make the SST $k-\omega$ model applicable in a wider range of flows than the standard model.

$$(\rho k)_{,t} + (\rho k u_i)_{,i} = (\Gamma_k k_{,j})_{,j} + \widetilde{G_k} - Y_k + S_k \tag{4.4}$$

$$(\rho \omega)_{,t} + (\rho \omega u_i)_{,i} = (\Gamma_\omega \omega_{,j})_{,j} + G_\omega - Y_\omega + D_\omega + S_\omega \tag{4.5}$$

In these equations $\widetilde{G_k}$ represents the generation of turbulent kinetic energy due to mean velocity gradients, G_ω represents the generation of ω, Γ_ω and Γ_k represent the effective diffusivity of ω and k, respectively. Y_k and Y_ω represent the dissipation of k and ω due to turbulence. D_ω represents the cross-diffusion term. S_k and S_ω are user defined source terms.

4.2 Airway Geometry

The airway geometries were given to us by the university of Antwerp. They performed two low radiation dose CT-scans on a patient, one at TLC, the other at FRC. Two scans at different levels make it possible to assess the relative lung expansion and therefore the relative mass fractions going to respective lobes can be estimated. Bifurcations up to the 7th generation were modelled. These

branches have a diameter of around 1 to 2 mm.

On closer inspection of the models one can see the inlet tube, the mouth, the larynx and the trachea with cartilage rings. The model then bifurcates into right main bronchi and left main bronchi. The left main bronchi (leading to the left lung) typically has a bent shape. See figure 4.1

The mesh was generated using the commercially available Tgrid and contains about $4 \cdot 10^6$ unstructured tetrahedral cells. Mesh independency studies have been performed by De Backer et al. [8], showing that very little difference (about 2%) was found in mass flow between a mesh with $1.5 \cdot 10^6$ cells and one with $4.5 \cdot 10^6$ cells. They chose a mesh size in between those mesh sizes to ensure good resolution in high gradient regions. The cells are clustered towards the wall. As Longest and Vinchurkar [18] note, it would be better to have a hexahedral mesh.

However because the model is derived from a CT scan that has a limitation in resolution, some problems occur in the geometry. Some branches leading to outlets are so short that the flow does not get the time to fully develop (see figure 4.4). This then results into reversed flow, thus making the solver unstable. It would be advisable in the future to elongate all outlets.

Also present are nonphysical indentations, as can be seen in figure 4.5.

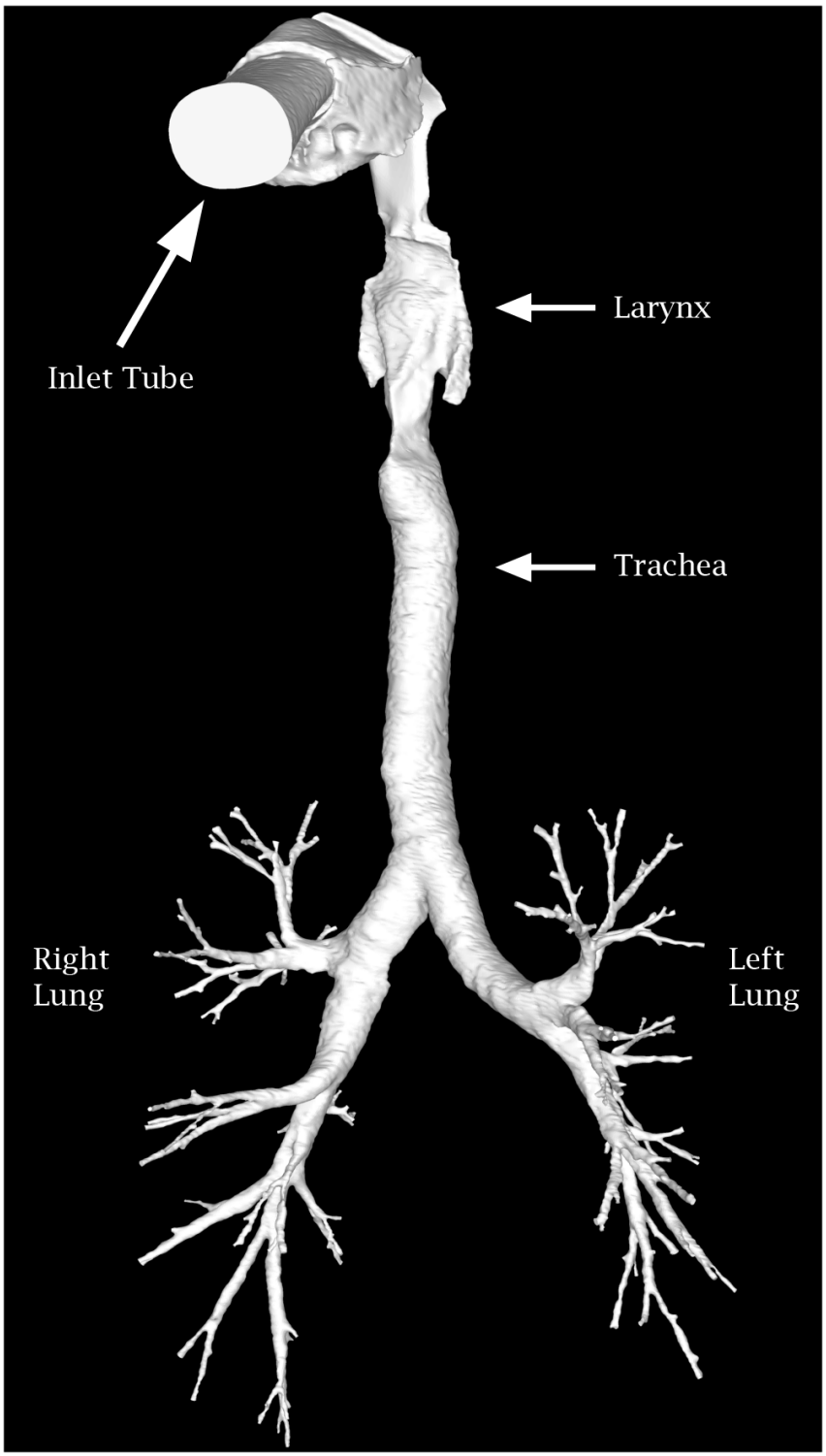

Figure 4.1: The full geometry.

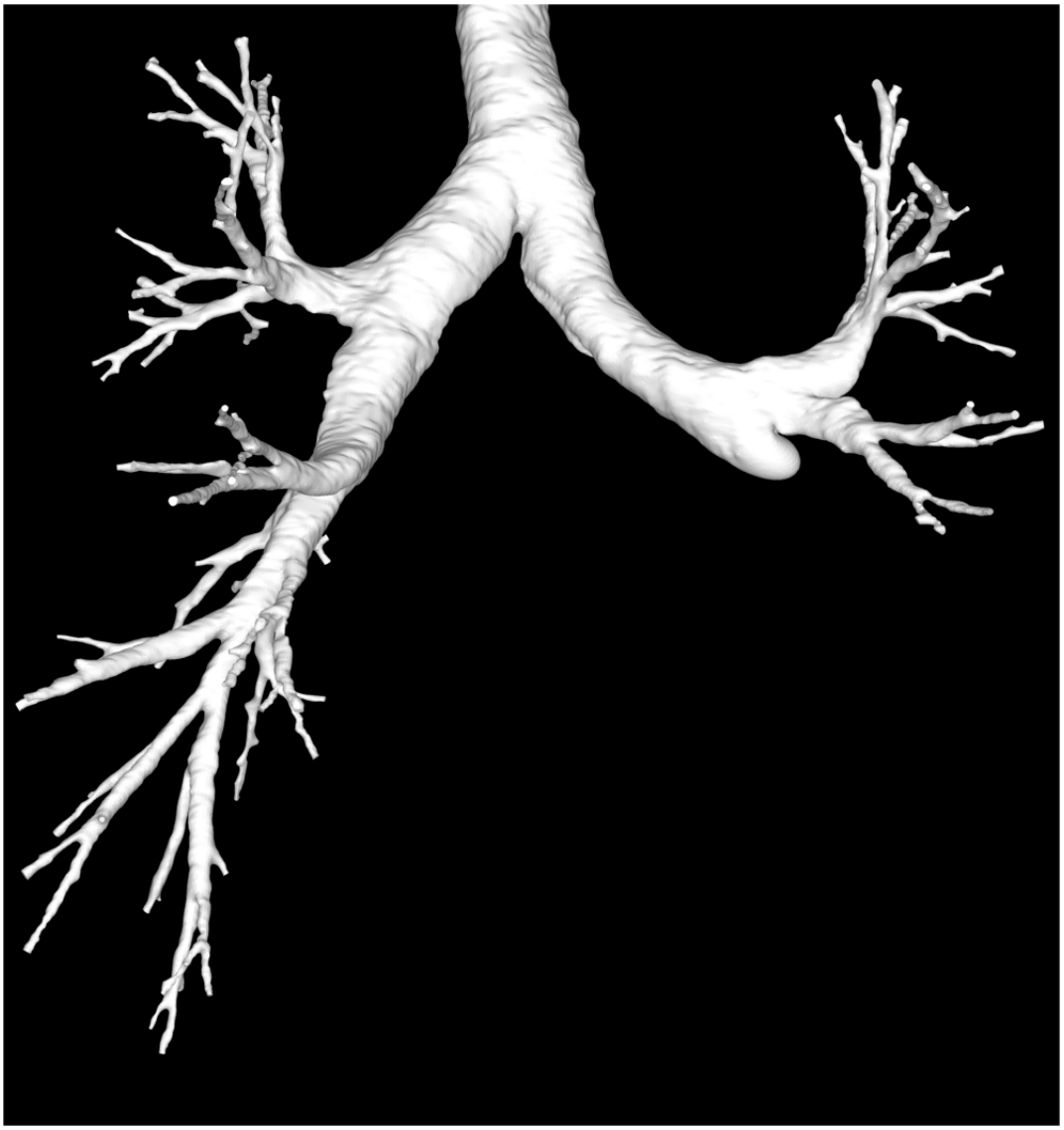

Figure 4.2: The geometry with the left lower lobe removed.

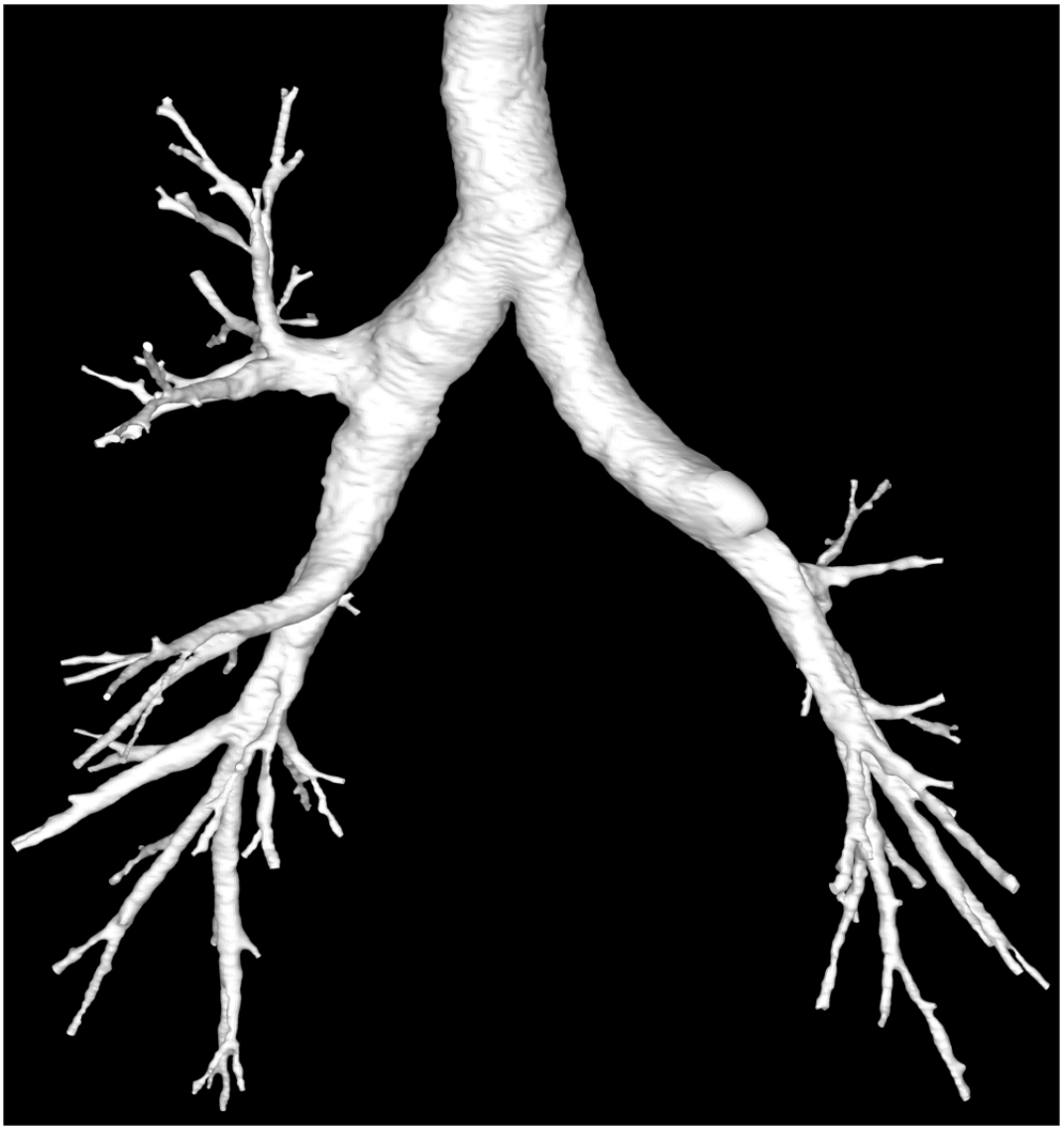

Figure 4.3: The geometry with the left upper lobe removed.

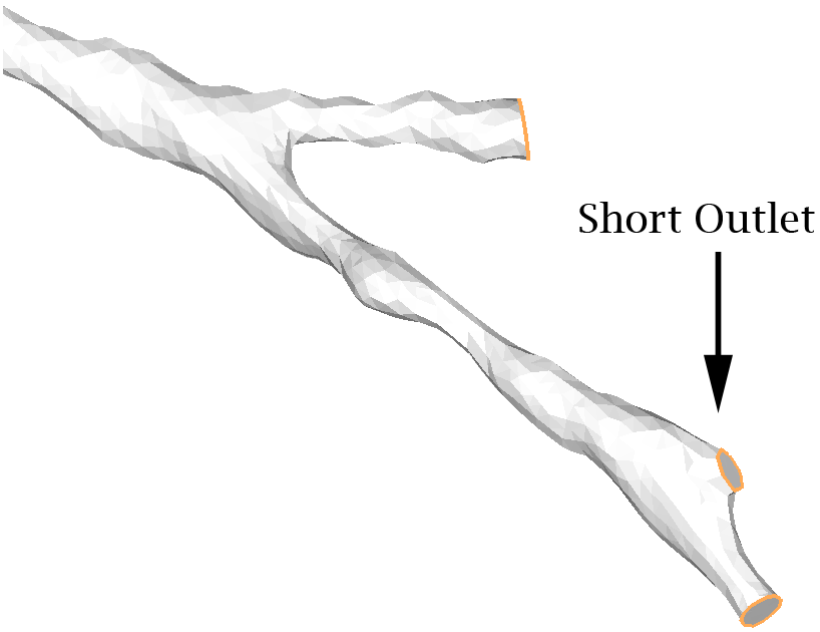

Figure 4.4: A short outlet.

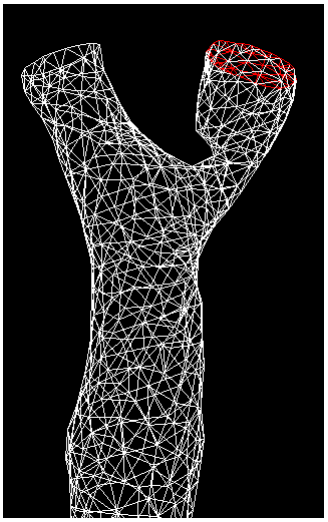

Figure 4.5: A nonphysical indentation.

4.3 Modelling the Flow

4.3.1 Fluid Flow

In the present thesis both laminar and turbulent simulations were carried out. Based on the work of Brouns [2] the SST $k-\omega$ transitional model was selected for its ability of $k-\omega$ to predict transitional flows.

Pressure Drops

Very little difference can be found between the left and right panels of figures 4.6 and 4.7. The median pressure drop difference between laminar and turbulent flow for 15 and 30 l/min was respectively 0.7 Pa and 7.5 Pa. This amounts to a mean increase in pressure between laminar and turbulent flow of respectively 1.5% and 5.8%.

Velocities

We then compared the flow field between laminar and turbulent cases.

Figure 4.8 demonstrates the locations of the cuts made to generate the velocity profiles. Cut a is just before the laryngeal jet, cut b is at the jet's center. Cuts c and d are further downstream.

Contour plots of the velocity are made for the central sagittal plane. To compare the different flow rates, the velocity has been normalized by dividing by the inlet velocity.

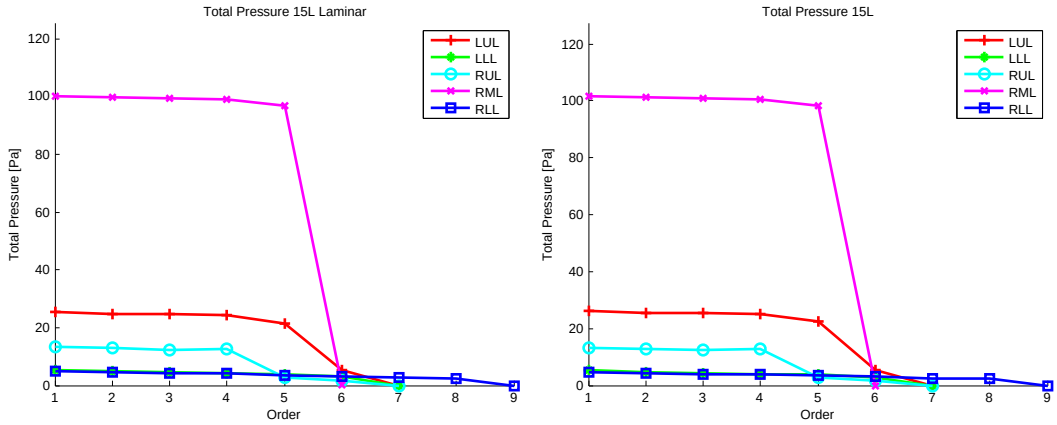

(a) Laminar **(b)** Turbulent

Figure 4.6: Comparison between laminar and turbulent flow of pressure drops at 15 l/min.

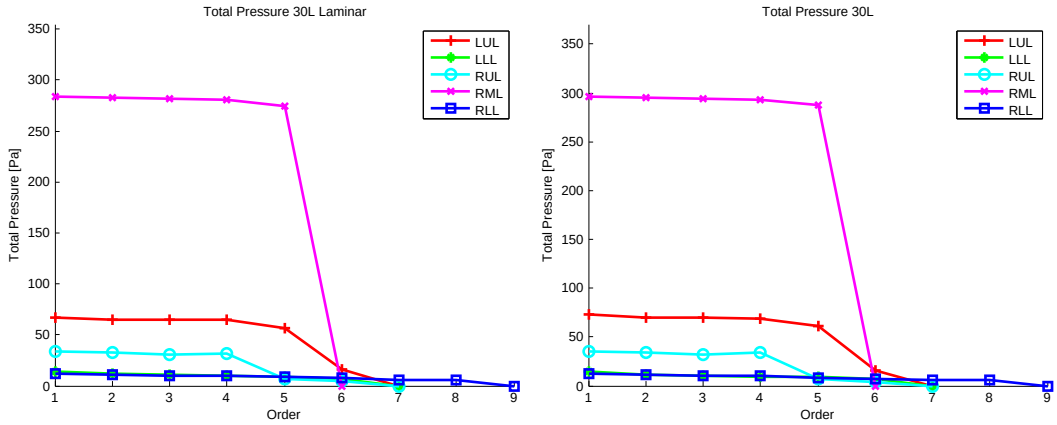

(a) Laminar **(b)** Turbulent

Figure 4.7: Comparison between laminar and turbulent flow of pressure drops at 30 l/min.

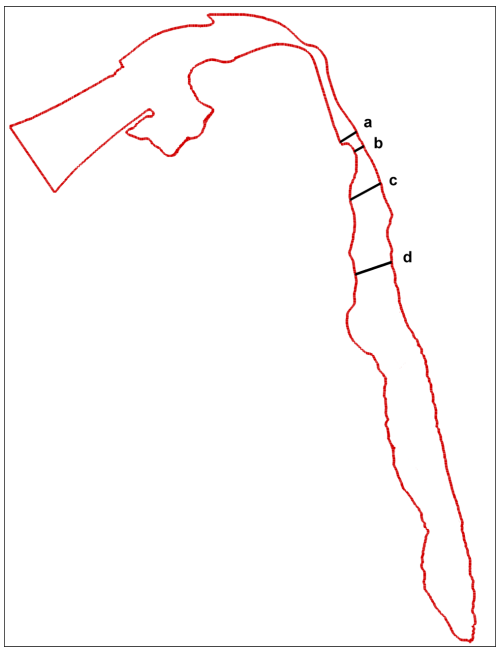

Figure 4.8: Location of the cuts for the velocity plots

Comparing laminar and turbulent velocities (figures 4.9 and 4.11) in panels (a) and (b) we see virtually no difference. This is to be expected, since turbulence only really occurs after the laryngeal jet. In panels (c) and (d) we see that some differences occur in velocity profile. The laryngeal jet is a little wider in the turbulent simulation. The jet has also moved a little more to the posterior side in the laminar case. This is best seen when comparing 30 l/min turbulent and laminar flow. In panel (d) a peak in velocity is present in laminar simulations around $\frac{X}{D} = 0.25$. This peak is not present in turbulent simulations.

When looking at the velocity contours (figures 4.10 and 4.12) one can see the high velocity region reaching the end of the trachea in the laminar case. In the

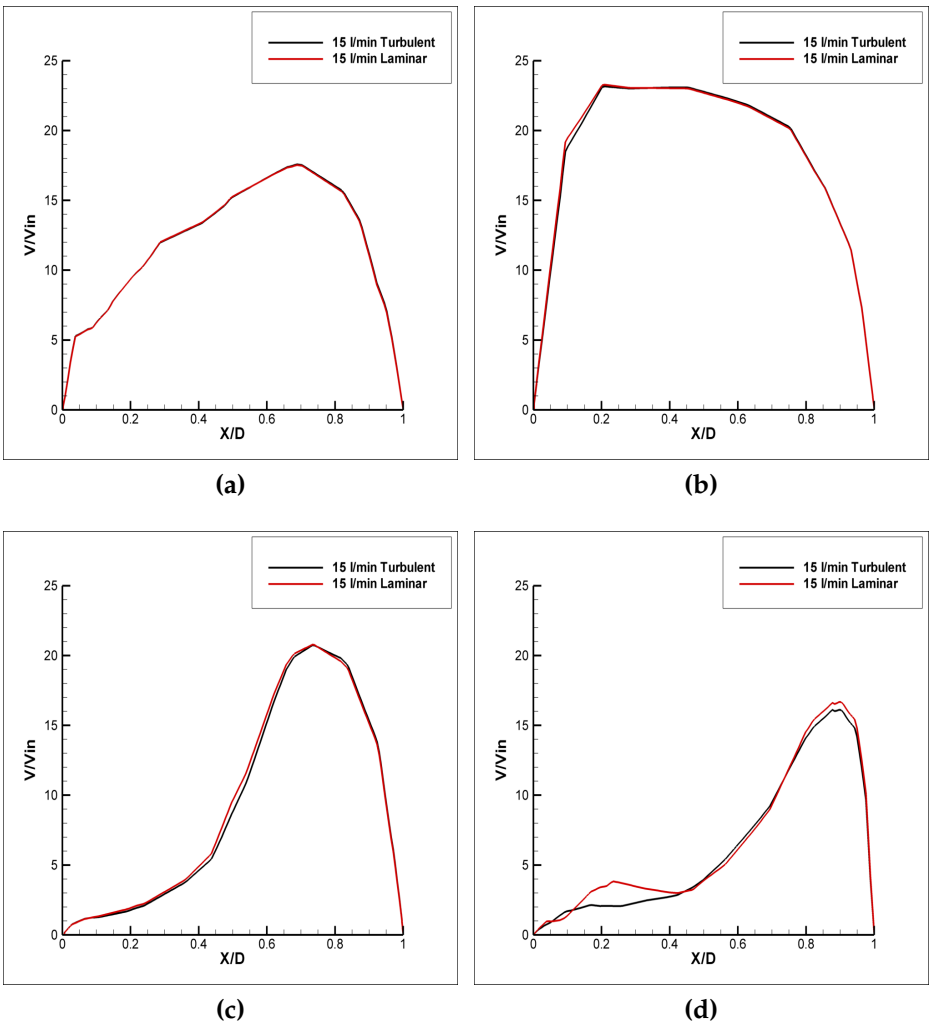

Figure 4.9: Comparison of velocity profiles.

turbulent case this region is smeared out before reaching the first bifurcation.

Even though there are limited differences in pressure drop we chose to use a turbulence model, because of the change in flow field that is present. If ever particle tracking would be done on this geometry, the change in shape of the laryngeal jet would certainly have an influence on the hot spot locations (i.e. locations where a lot of deposition takes place).

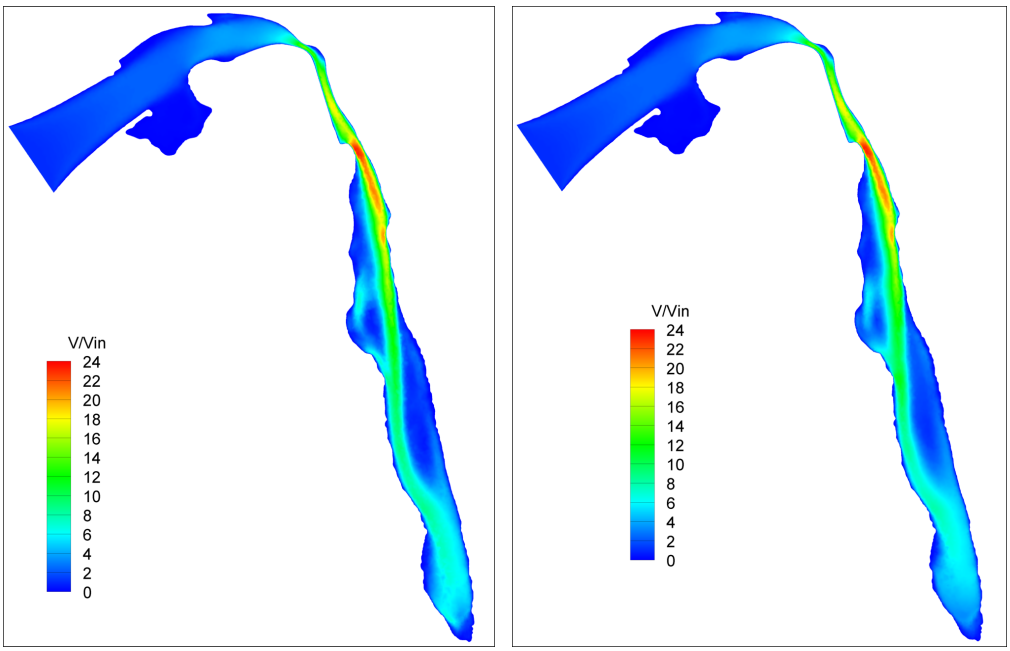

(a) Laminar **(b)** Turbulent

Figure 4.10: Velocity contour for 15 l/min.

It should be noted that we used mass fractions outlets for both the laminar and turbulent simulations. We later changed the boundary conditions, but the conclusion still stands, as almost no differences are found between the flow field in the trachea on which we based our decision to select a turbulence model.

4.3.2 Fluid

The air was considered to be homogeneous, isothermal, incompressible and Newtonian.

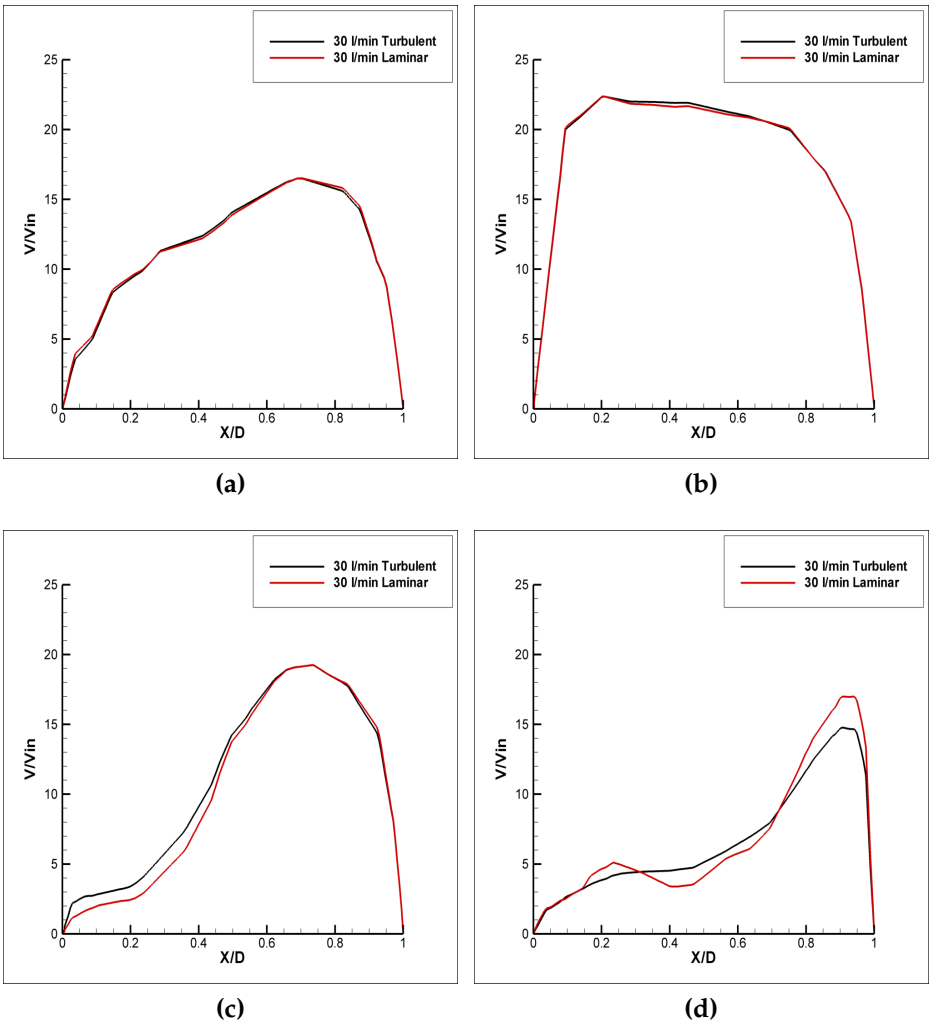

Figure 4.11: Comparison of velocity profiles.

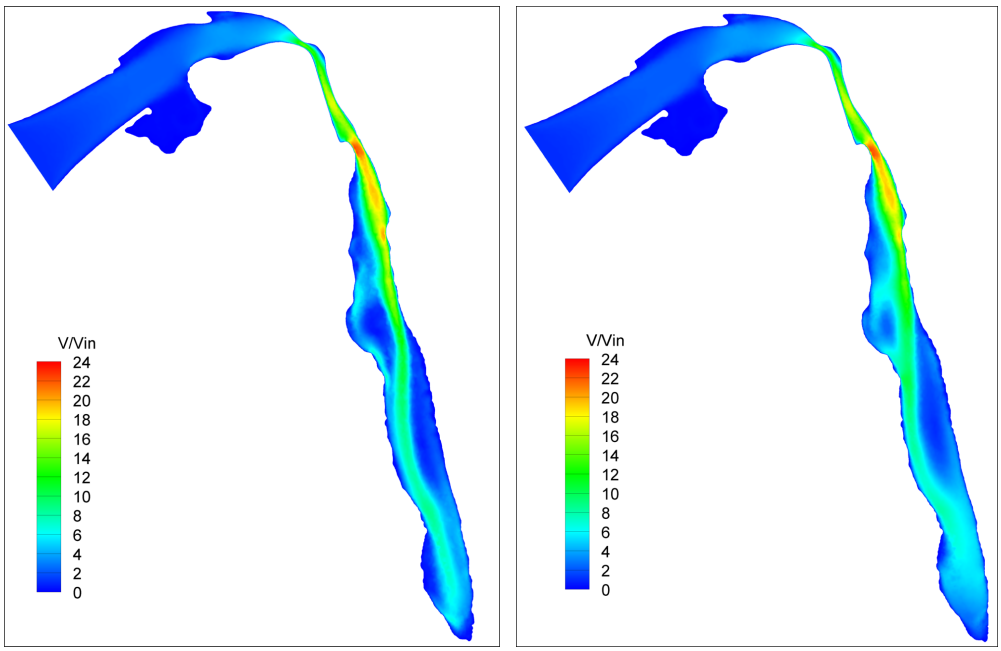

(a) Laminar **(b)** Turbulent

Figure 4.12: Velocity contour for 30 l/min.

4.3.3 Inlet

At the inlet some information needs to be provided. A mass flow inlet was used allowing us to quickly change the breathing level (i.e the amount of air taken in per minute). The different breathing levels that were studied were 15, 30, and 60 l/min. These levels correspond to respectively being at rest, light activity and heavy activity. Since these are volumetric flows, they have to be converted to mass flow per second, but since we know the density, this is not a problem.

Turbulence Parameters

The turbulence parameters [1] are to be given at the inlet. The inlet can be approximated by an ellipse. Using 4 points and their coordinates the approx-

imate length of the major and minor axis were determined.

$$P = 4aE(1 - \frac{b^2}{a^2}) \tag{4.6}$$

$$E = \sqrt{1 - \frac{b^2}{a^2}} \tag{4.7}$$

Here, a is the length of the major axis, b the length of the minor axis, P the perimeter of the ellipse and E the eccentricity. The area A of the inlet can be exported from Fluent. Using the area A and the perimeter P the hydraulic diameter D_h can be determined.

$$D_h = \frac{4A}{P} \tag{4.8}$$

From this the turbulence intensity can be calculated using:

$$v_{avg} = \frac{\dot{m}}{\rho A} \tag{4.9}$$

$$Re_{D_h} = \frac{\rho v_{avg} D_h}{\mu} \tag{4.10}$$

$$I = 0.16(Re_{D_h})^{-\frac{1}{8}} \tag{4.11}$$

Here, ρ is the density, $\dot{m}$ the mass flow, v_{avg} the average velocity of the flow, μ the dynamic viscosity and I the turbulent intensity.

Using the turbulence intensity we then calculate the turbulent kinetic energy.

$$k = \frac{3}{2}(v_{avg}I)^2 \tag{4.12}$$

Only the ω parameter is still to be determined.

$$\omega = \frac{\sqrt{k}}{C_{\mu}^{\frac{1}{4}}\rho} \tag{4.13}$$

With $C_{\mu} \approx 0.09$.

However Heenan et al. [12] noted that these turbulence parameters have little influence on the results.

4.3.4 Outlet

Choosing the outlet boundary condition is the most critical choice to be made. We need to satisfy the information we have at hands: the mass fraction to each lobe. The two big options we have are pressure outlets and outflows with set mass fraction. However we do not have information available on the mass fraction through each outlet, since the mass fractions are given on a lobar level, and we do not have pressures at the outlets.

Entire Lung

Using the mass fraction that is given for each lobe and knowing how many outlets every lobe has we can estimate the mass fraction that is going through each outlet by dividing the mass fraction of the lobe by its number of outlets. However using this approach we force flow through small outlets (4.13) res-

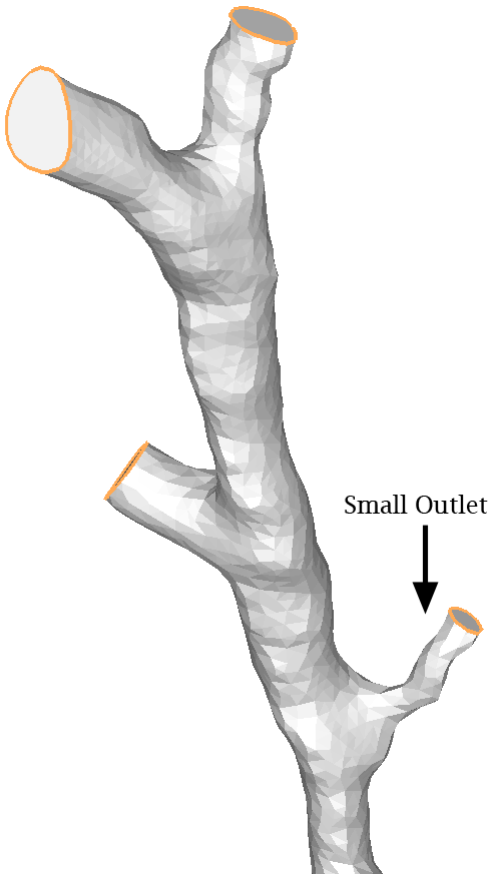

Figure 4.13: Example of a small outlet.

ulting in unrealistic pressure drops at some outlets. This problem was also reported by Luo and Liu [19] and caused them to switch to pressure outlets.

An attempt was made to resolve the issue of forcing a relatively large mass flow through a small outlet by using a weighted average over the outlet area. This did solve the problem at some locations, but also worsened it at others, or even created new problems at still other locations. This can be seen when comparing the middle and right panel between figures 4.14 and 4.15. For example if we compare panel (b) of figures 4.14 and 4.15, we do not observe

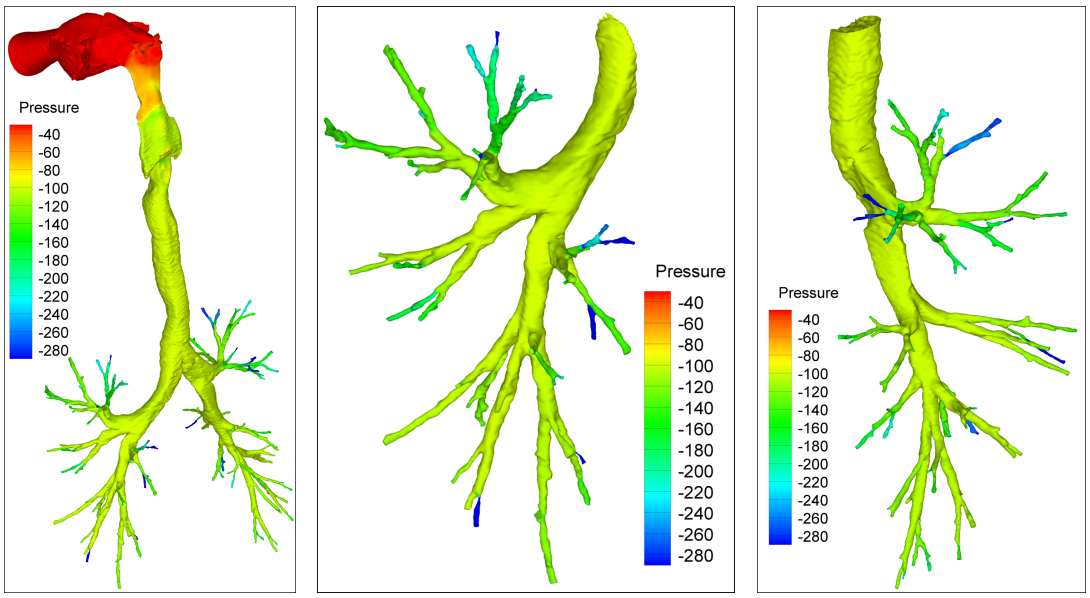

(a) Full Geometry **(b)** Left Lung **(c)** Right Lung

Figure 4.14: Global view of pressure drops for 30 l/min with mass fraction outlets.

a big pressure drop at the left middle of panel (b) of figure 4.14. However, when we look at panel (b) of figure 4.15, there is a sudden pressure drop. The opposite can also be seen. Looking at the right top corner of panel (c) we can see that a large pressure drop was resolved using weighted average mass fraction outlets.

After closer inspection it became clear that the new problems are a the result of large outlets that are constricted by a small section. An example of this is illustrated in 4.16.

We then switched to using pressure outlets. The pressures for all outlets of one lobe were set uniformly. We then iteratively tried to match the mass distribution to the information by changing the pressures at different lobes. (This

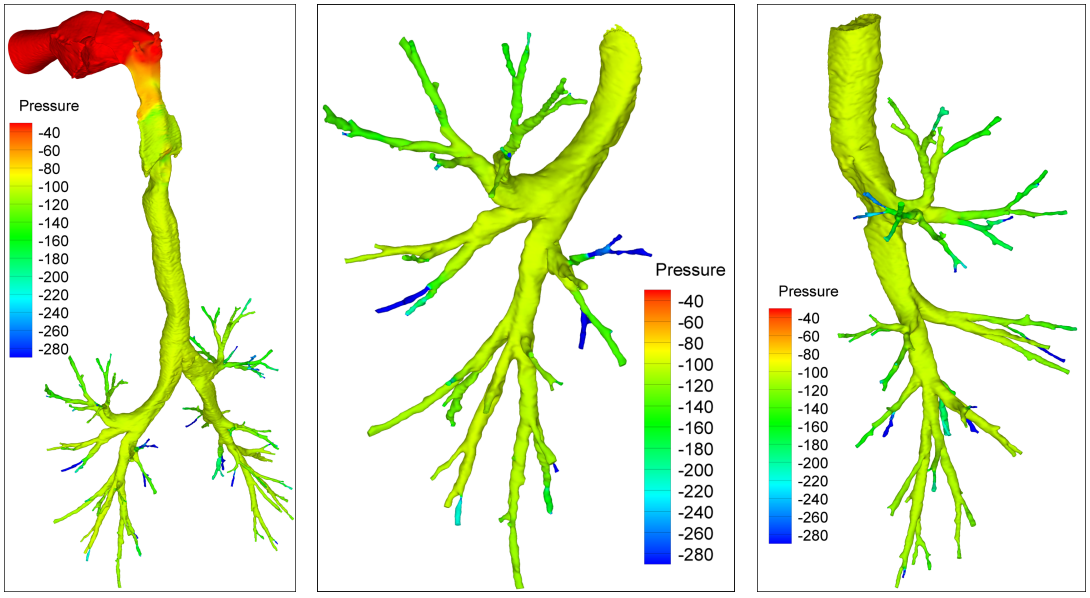

(a) Full geometry **(b)** Left lung **(c)** Right lung

Figure 4.15: Global view of pressure drops for 30 l/min with weighted mass fraction outlets.

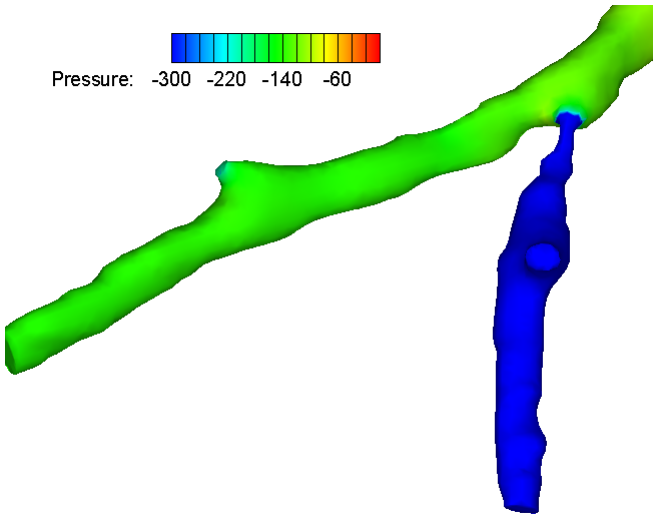

Figure 4.16: Example of forced flow through a small section.

was suggested by De Backer et al. [8].) This is a slower (in the sence that it takes more human interaction) but more realistic condition, as in reality the flow is driven by a lower pressure. This also solves most of the problems. Small outlets will get less mass flow and constricted outlets will get less flow.

Our pressure outlet distribution was started from the average pressure at the outlets of a lobe, computed using the mass fraction approach. The outliers that resulted from a forced flow were removed from the average. Then the left/right distribution was adjusted by increasing the pressure drop in the lobe having the biggest shortage of mass in the lung that receives too little air. In the lung that received too much air, the pressure drop was decreased in the lobe having the largest surplus of air supplied. Once the left/right distribution was acceptable, the mass distribution within the two lungs was tackled using the same procedure.

Figure 4.18 takes another look at the pressure drops. It should be noted that the pressure drop between the mouth and the first bifurcation is not included in these graphs. It can be seen that there is a large pressure drop between the 5^{th} and the 6^{th} bifurcation on the left panel. In panel (b) this problem is not resolved and a new problem has been created. All problems are resolved by using pressure outlets. Comparing panel (b) of 4.18 with figure 2.1 we can see that we have the same magnitude of pressure drop.

It can be seen in figure 4.19 that the mass flow divides approximately evenly after every bifurcation, as could be expected. It can also be seen that there is

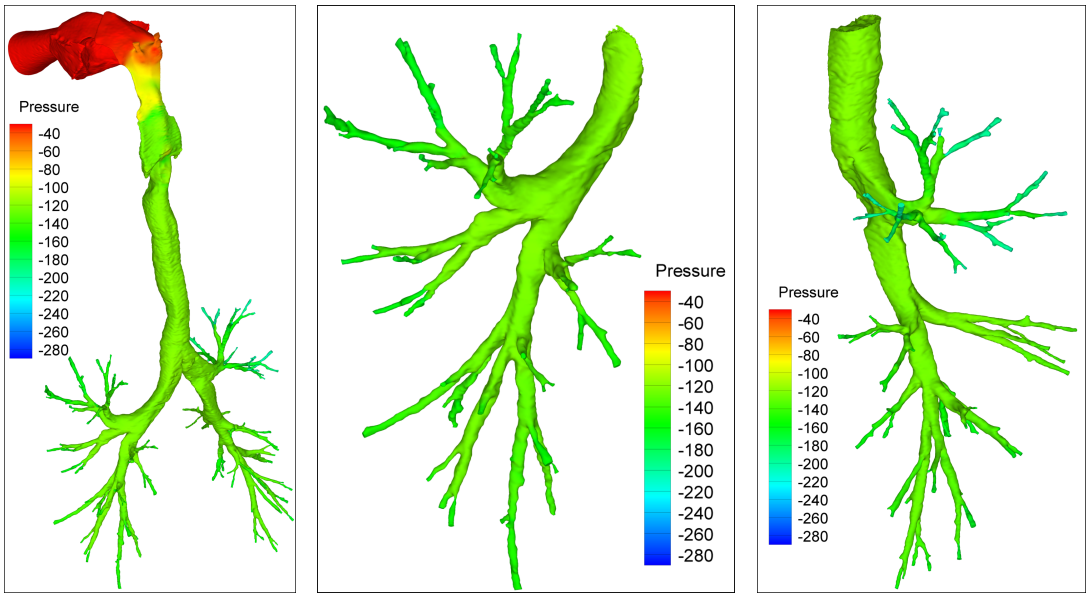

(a) Full geometry **(b)** Left lung **(c)** Right lung

Figure 4.17: Global view of the pressure drops for 30 l/min with pressure outlets.

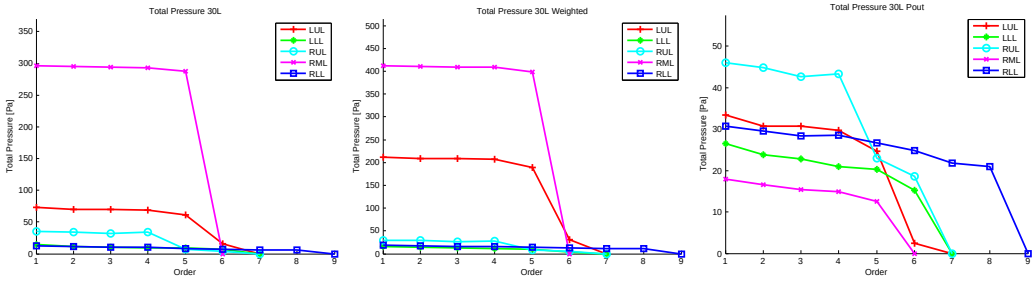

(a) Mass fraction outlets **(b)** Weighted mass fraction outlets **(c)** Pressure outlets

Figure 4.18: Pressure drop comparison for the 30 l/min case.

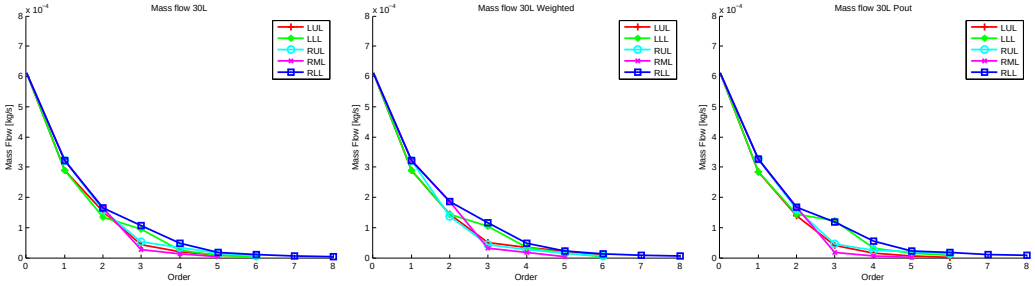

(a) Mass fraction outlets **(b)** Weighted mass fraction outlets **(c)** Pressure outlets

Figure 4.19: Comparison between different mass distributions for different boundary conditions for 30 l/min.

a difference along the pathway between the different outlets. This can also be expected since we now only control mass flow at a lobar level and the mass flow distributes itself according to the geometry in the lobe.

Another option for boundary conditions could be to impose the sum of the mass fractions through the different outlets of a lobe to be equal to the mass flow of the lobe. This however is not straightforward to implement, since it involves writing a user defined function and advanced knowledge of Fluent.

Lungs with Lobes Removed

Since one of the long term goals is to predict lung function after lobectomy, we should be able to predict flow in a lung model with a lobe removed. However, we do not know anything about the flow field. How does the flow redistribute? Does it simply add the volume to the other lobes, or are there more complex changes?

We decided to take the pressure outlet boundary conditions we obtained using the full geometry and to look at what happens with the mass flow distribution. We should however note that as long as no experimental data is available, we cannot determine whether the attained results are physically correct. Additionally the geometry may change significantly due to the removal of a lobe, rendering predictions even more difficult.

4.3.5 Wall

At the wall a no slip condition is imposed.

4.4 Solver Settings

Other than boundary conditions we also need to provide the solver with numerical schemes, relaxation factors and some other settings. Lots of different settings have been tried, but only a few of them led to convergence.

4.4.1 Numerical Schemes

The following settings led to a converged solution in almost all cases. When convergence issues arose, it generally helped starting with the default schemes and then increasing the order of the schemes.

- Pressure: 2^{nd} Order
- Momentum: 2^{nd} Order Upwind
- Turbulent Kinetic Energy: 3^{rd} Order Upwind

- Specific Dissipation Rate: 3^{rd} Order Upwind

These schemes were used for both mass flow outlets and pressure outlets. The highest residuals were on the order of 10^{-3}.

4.4.2 Relaxation Factors

The relaxation factors were left unchanged.

- Pressure: 0.3
- Density: 1
- Body Forces: 1
- Momentum: 0.7
- Turbulent Kinetic Energy: 0.8
- Specific Dissipation Rate: 0.8
- Turbulent Viscosity: 1

4.4.3 Miscellaneous

The pressure-velocity coupling used was SIMPLE. SIMPLEC sometimes gave better convergence but was more unstable and did not always converge.

Even though Fluent suggested using node based gradients, convergence was more stable using cell based gradients.

4.5 Conclusions

The geometry, turbulence model, boundary conditions and solver settings all play their part in a very complex and sometimes confusing way to reach a good and reliable solution.

There are some issues with the geometry. Short outlets and sharp edges that are likely not physical, impede convergence by generating reversed flow. These issues could be solved by elongating all outlets. This would eliminate all reversed flow without disturbing the upstream flow field. Keeping in mind possible particle tracking at some later stage, we preferred a turbulent model above the faster laminar case.

After trying several options for boundary conditions it would appear that pressure outlets are the only viable option, since all other options featured some unrealistic pressure drops.

The solver settings have also been determined.

CHAPTER

FIVE

RESULTS

Due to the complexity of the geometry, it is very difficult to show results in a clear way. One cut was made through the middle of the trachea (central sagittal plane) in order to visualize the laryngeal jet.

Visualizing results further downstream of the trachea is difficult. Several cuts are made along selected paths down the airway. It was made sure that at least one path per lobe extends to the edges of the model. To characterize one branch of the airway at least 2 slices are necessary, one at the entrance and one at the exit (just before the next bifurcation) of the branch. Figures 5.1 and 5.2 show these slices and the resulting paths. These sections are also used in the lungs with lobes removed.

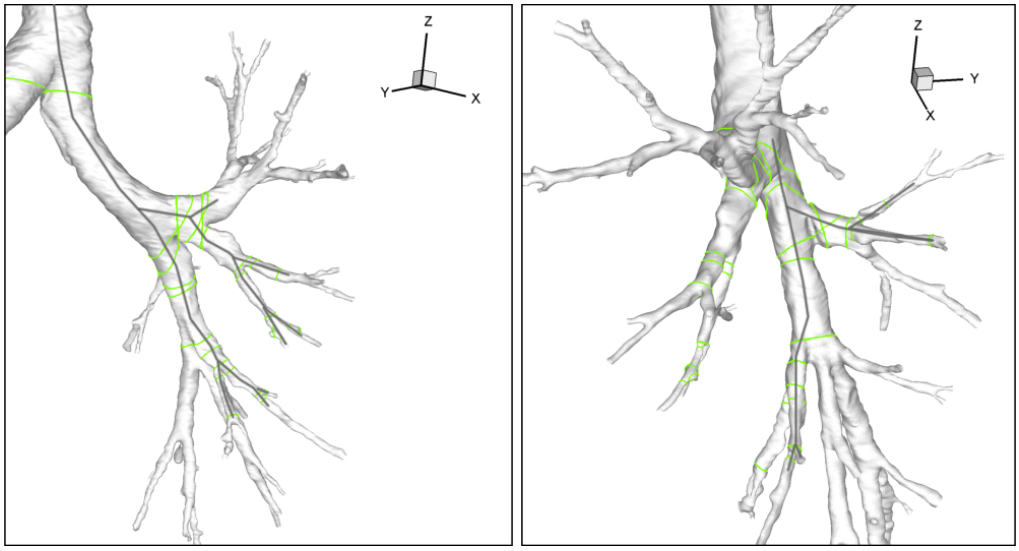

Figure 5.1: Paths down the left lung.

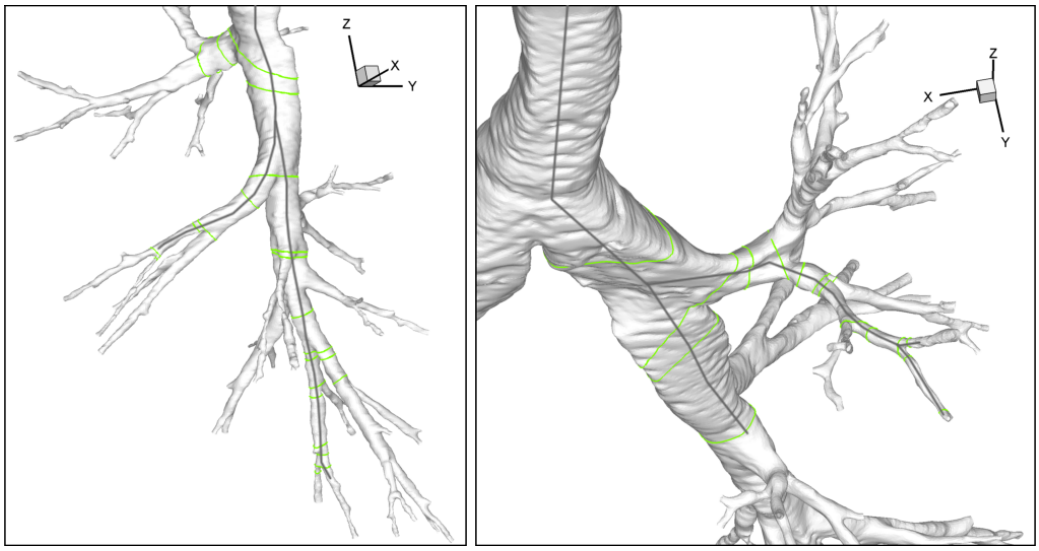

Figure 5.2: Paths down the right lung.

5.1 Full Geometry

5.1.1 Velocity

When studying figure 5.3 we can see that the relative velocities are a little lower in the jet at higher flow rates (see panel (b)). On panel (c) we see that the jet becomes less pronounced with increasing flow rate. The same phenomenon is observed in panel (d). On this panel we can also see that the velocity downstream of the jet becomes more and more uniform as flow rate increases.

When comparing the velocity contours (figures 5.4, 5.5 and 5.6), we see that the laryngeal jet becomes shorter, wider and less pronounced with increasing flow rate.

5.1.2 Pressure Drops

Again it should be noted that the pressure drop over the trachea is not included in figure 5.7. One can observe that panels (a), (b) and (c) are very similar. The scale on the y-axis increases with increasing flow rate, but the largest pressure drop always takes place at the same location.

In figures 5.8, 5.9 and 5.10 we can make the same obervation. The pressure drops become bigger, but the locations do not change.

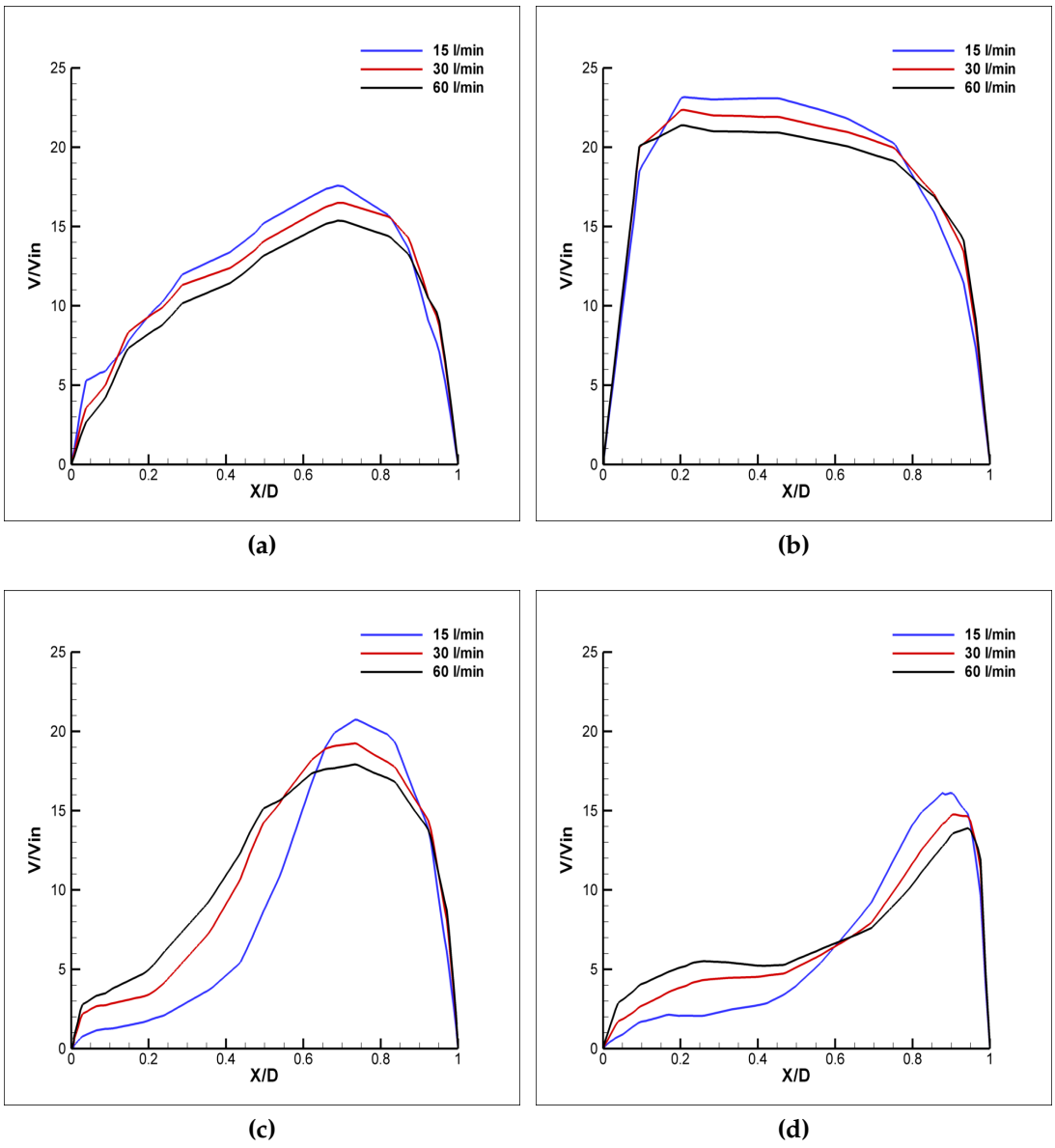

Figure 5.3: Comparison of the velocity profiles.

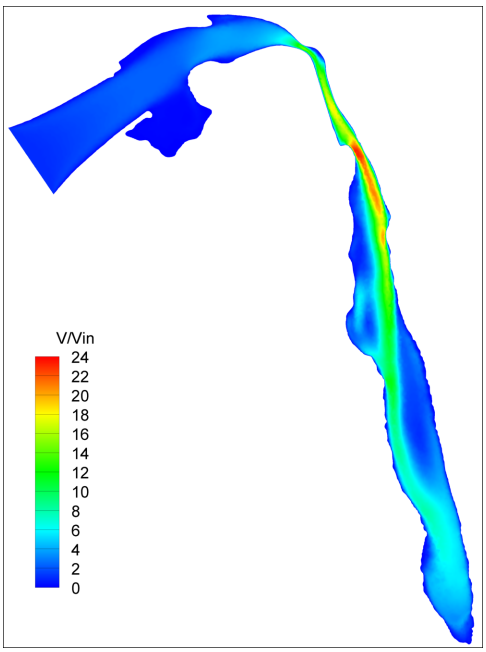

Figure 5.4: Velocity contour for 15 l/min pressure outlet case.

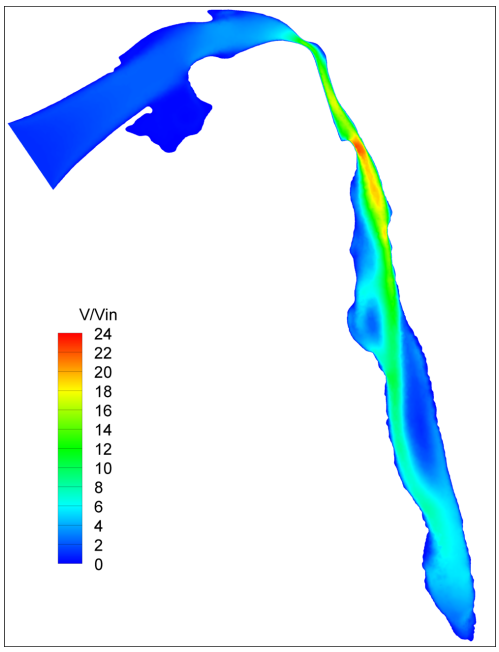

Figure 5.5: Velocity contour for 30 l/min pressure outlet case.

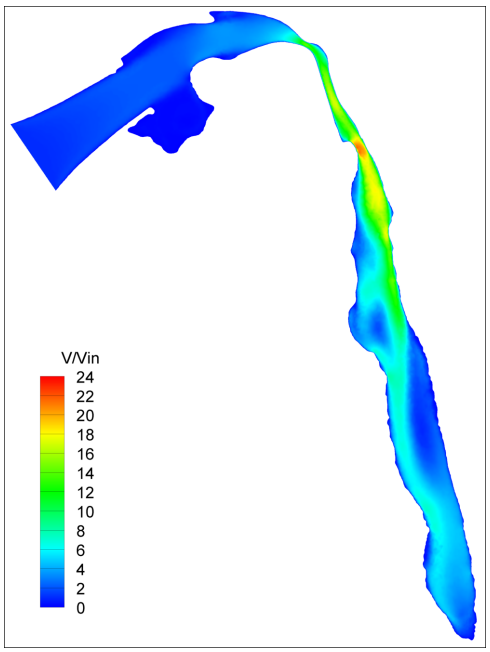

Figure 5.6: Velocity contour for 60 l/min pressure outlet case.

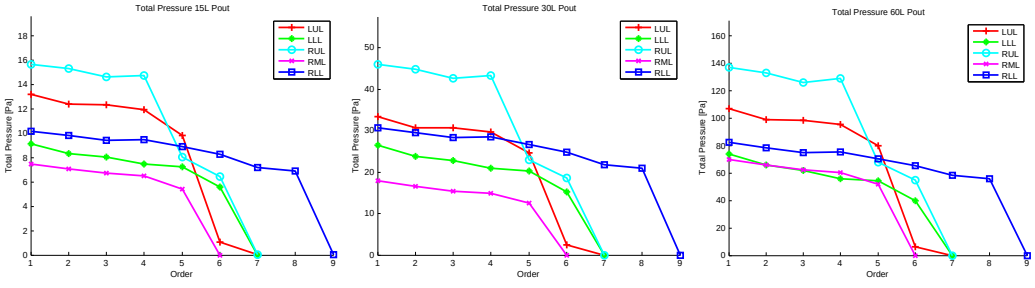

(a) 15 l/min **(b)** 30 l/min **(c)** 60 l/min

Figure 5.7: Pressure drops along selected pathways.

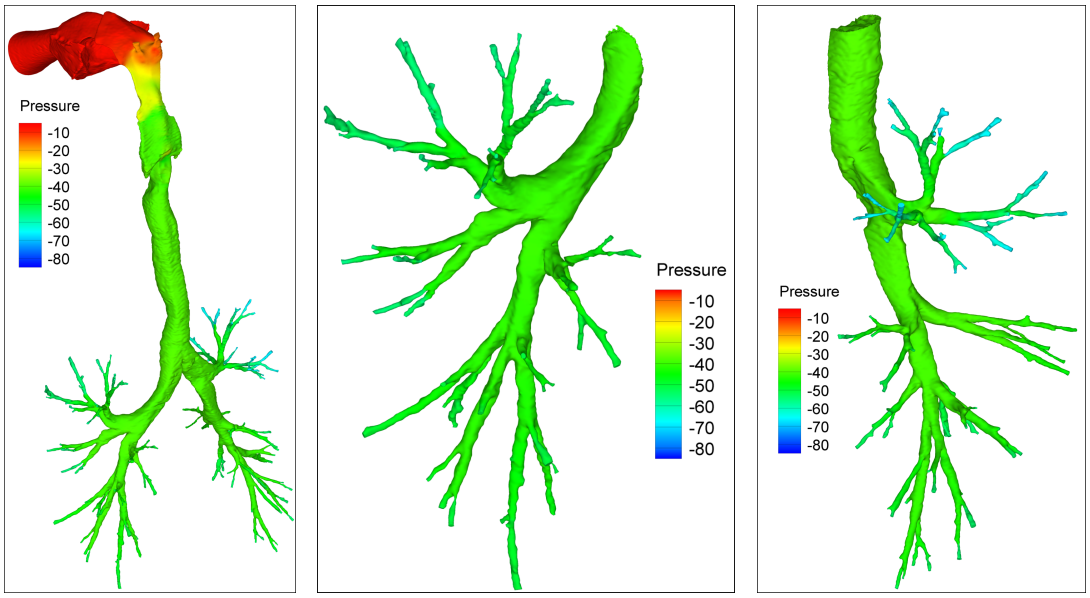

(a) Full geometry **(b)** Left lung **(c)** Right lung

Figure 5.8: A global picture of the pressure drops at a flow rate of 15 l/min.

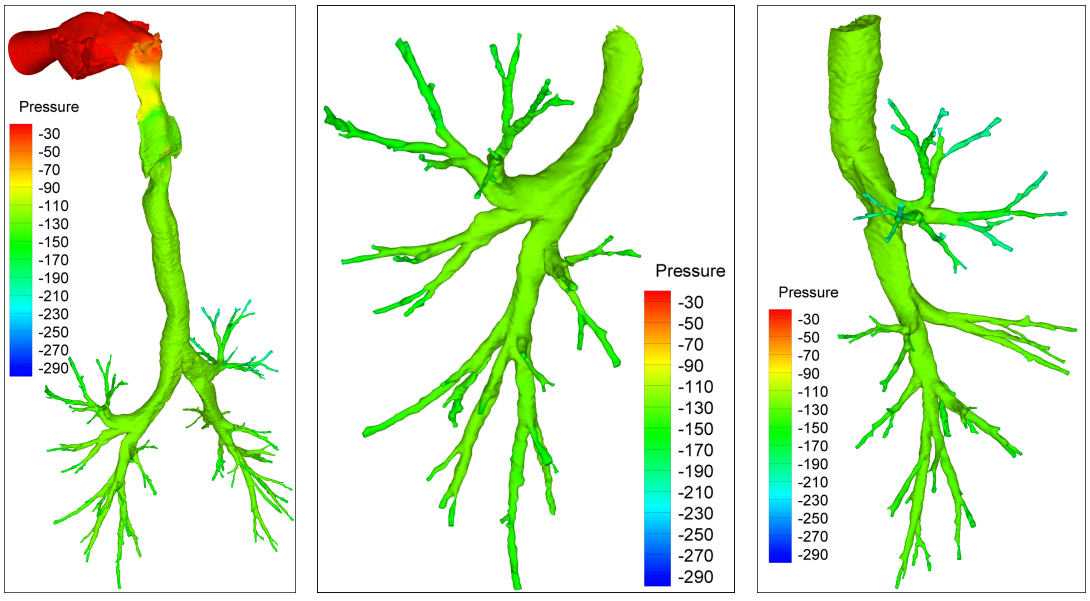

(a) Full geometry **(b)** Left lung **(c)** Right lung

Figure 5.9: A global picture of the pressure drops at a flow rate of 30 l/min.

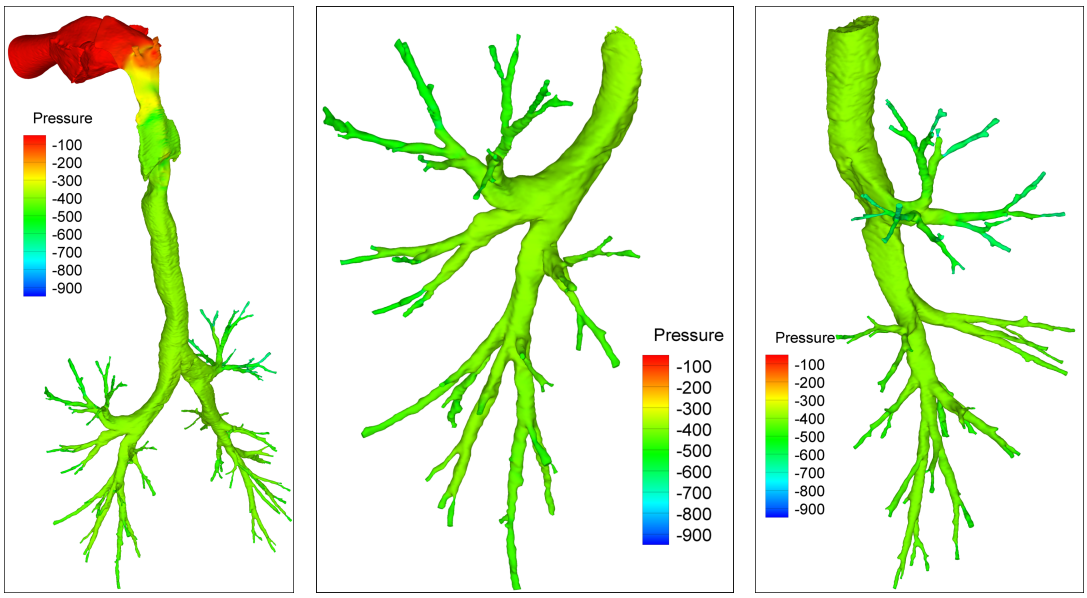

(a) Full geometry **(b)** Left lung **(c)** Right lung

Figure 5.10: A global picture of the pressure drops at a flow rate of 60 l/min.

5.1.3 Resistance

The resistance in the airways is defined in analogy with the resistance in an electrical network.

$$R = \frac{\Delta P}{\dot{m}} \tag{5.1}$$

with R the resistance, ΔP the pressure drop and $\dot{m}$ the mass flow.

When looking at figure 5.11 the first thing that one notices is the huge spike present in all three panels. Since we fixed the pressure drop, this spike can only have one cause: the mass flow passing through the studied portion of the lung has suddenly dropped very steeply. Looking at the geometry in figure 5.12, we can see that this is indeed physical. The diameter of the studied airway has suddenly dropped by a factor 4, decreasing the area by about 16.

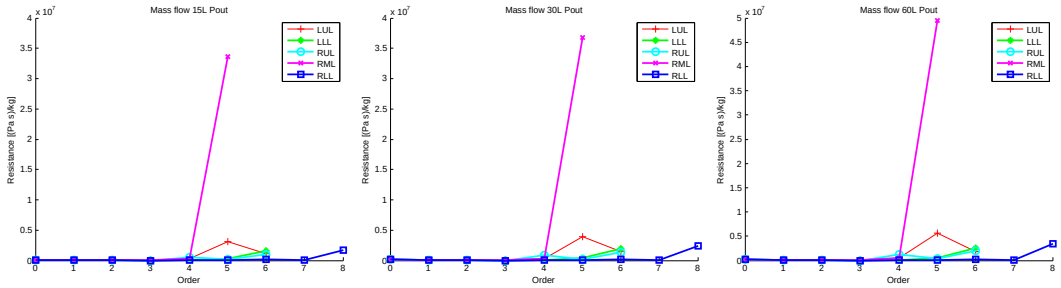

(a) 15 l/min **(b)** 30 l/min **(c)** 60 l/min

Figure 5.11: A comparison of the resistance at different flow rates.

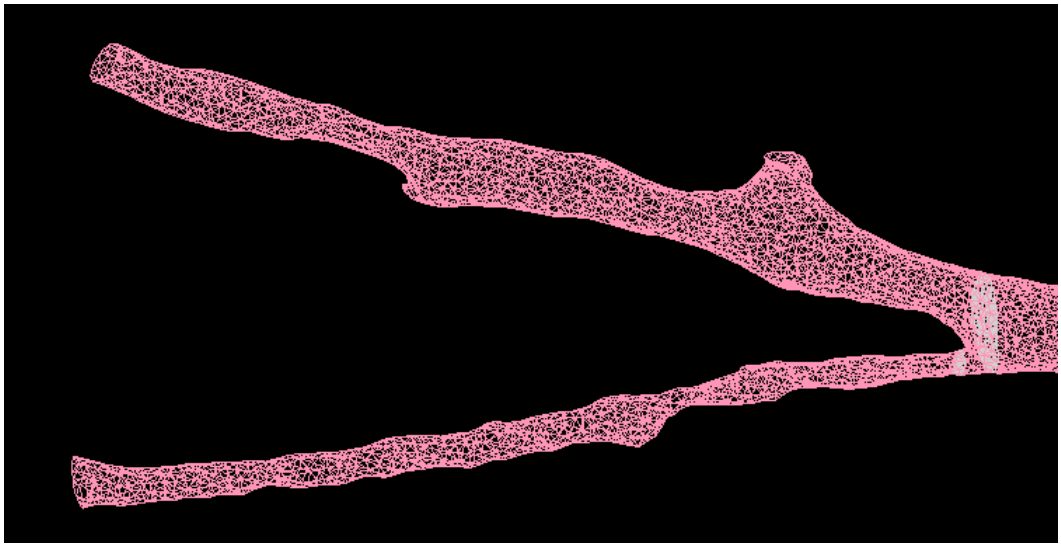

Figure 5.12: The outlet responsible for the spike in resistance seen in figure 4.18.

The largest part of the mass flow will thus flow through the much wider other branch, leaving the studied branch with very little.

It would have been interesting to look at the total resistance of the lung and the resistances of the lobes, but because of the complex geometry and the difficulty to create slices, this was not possible.

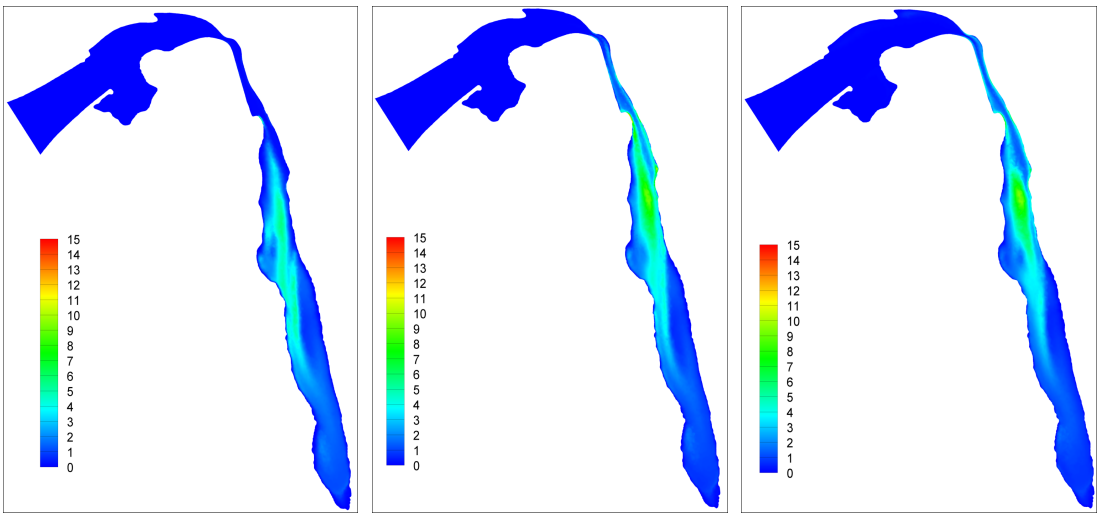

(a) 15 l/min **(b)** 30 l/min **(c)** 60 l/min

Figure 5.13: Normalized turbulent kinetic energy for the pressure outlet cases.

5.1.4 Turbulent Kinetic Energy

The turbulent kinetic energy can be seen to dissipate faster when flow rates are higher.

5.2 Lung with Lobes Removed

Two simulations were undertaken, one with the left upper lobe removed, and one with the left lower lobe removed. Both were done at 30 l/min.

5.2.1 Mass Fractions

Looking at figure 5.14 in panels (a) and (b) we can see a flat line between the first and second bifurcation, which results from the removal of a lobe; All air that goes in the left lung, goes to the remaining lobe.

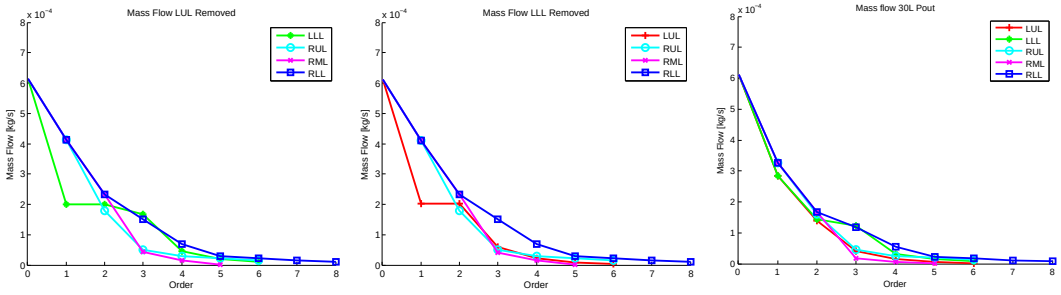

(a) LUL removed **(b)** LLL removed **(c)** Full lung

Figure 5.14: Mass flow in resected lungs.

In figure 5.15 the increase in mass fraction is studied.

$$\%mass\ fraction = 100\frac{\dot{m}_{lobe\ removed} - \dot{m}_{full\ lung}}{\dot{m}_{full\ lung}} \tag{5.2}$$

The mass fraction in the left lung has decreased, which is as we expect, as a lobe of the left lung has been removed. The mass fraction in the remaining lobe, however, has increased. The mass fraction in the right lung has also increased. We can also see, that the further we go down the lung, the mass fraction increase becomes smaller as the air spreads itself throughout the entire lung.

5.2.2 Pressure Drop

When comparing panels (a) and (b) with panel (c) from figure 5.16, we see that the total pressure drop increases for all remaining lobes. This is a logical result of forcing air through less area, thereby increasing velocity and thus total pressure. The largest increase can be seen in the right middle lobe. Looking at panels (a) and (b) we see that it makes virtually no difference whether we

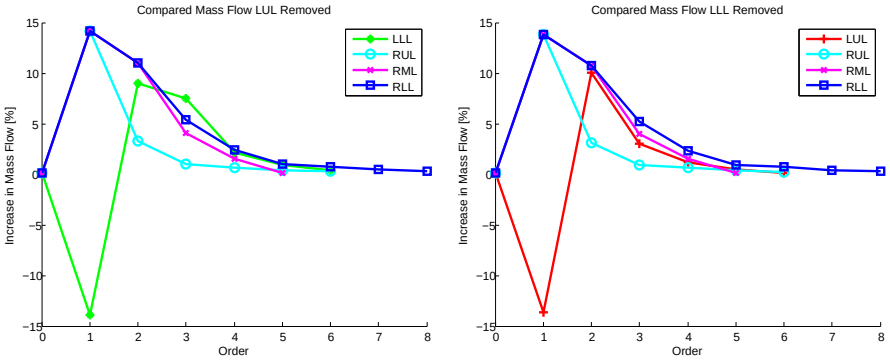

(a) LUL removed **(b)** LLL removed

Figure 5.15: Comparison of mass flow in resected lungs between full lungs and resected lungs.

	Full Lung	LUL Removed		LLL Removed	
	$\dot{m}/\dot{m}_t$	$\dot{m}/\dot{m}_t$	increase	$\dot{m}/\dot{m}_t$	increase
Left Lung	47.3%	32.6%	−13.9%	33.0%	−13.6%
LUL	25.2%			33.0%	10.1%
LLL	22.1%	32.6%	9.0%		
Right Lung	52.7%	67.4%	14.2%	67.0%	13.9%
RUL	28.8%	29.2%	3.2%	29.1%	3.1%
RML	4.5%	6.9%	4.1%	6.8%	4.0%
RLL	22.4%	32.3%	5.4%	31.1%	5.3%

Table 5.1: Growth in mass fraction.

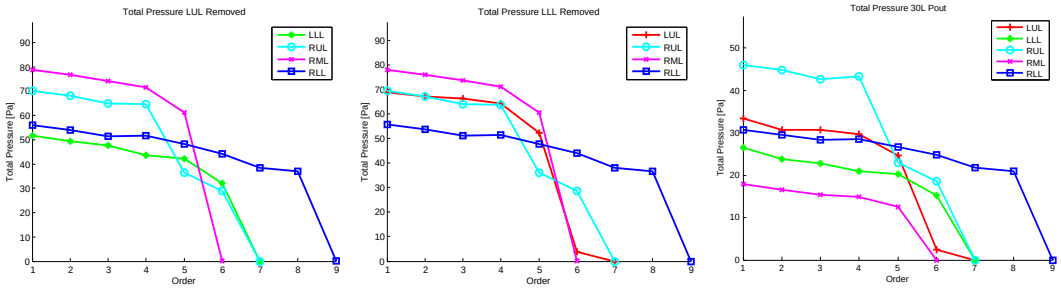

(a) LUL removed **(b)** LLL removed **(c)** Full lung

Figure 5.16: Pressure drop in resected lungs.

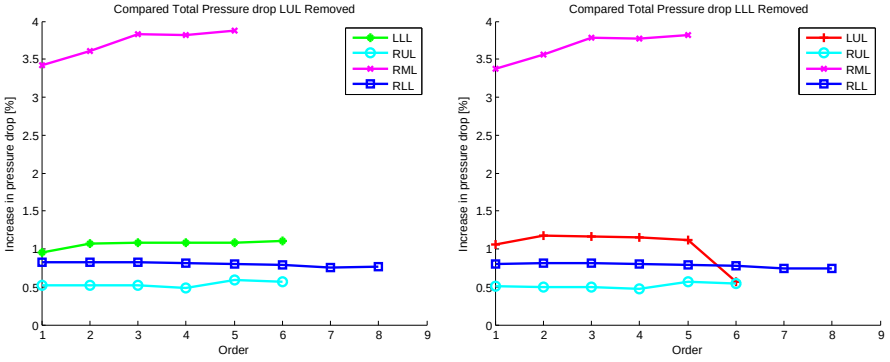

(a) LUL removed **(b)** LLL removed

Figure 5.17: Comparison of mass flow in resected lungs between full lungs and resected lungs.

remove the upper or lower lobe of the left lung: pressure drops in the right lung stay the same for both cases.

In figure 5.17 the large increase in pressure in the right middle lobe is striking.

5.3 Experimental Validation

Even though in the project experimental validation will be done by the Hogeschool Gent, we did not receive any data in time to include a comparison

of experimental and CFD results.

5.4 Conclusion

Using the pressure outlet boundary condition, we were able to attain realistic results for both the full lung geometry and the resected geometries. Nonetheless caution has to be taken, as no experimental validation has been done, especially with the geometry with lobes removed.

CHAPTER

SIX

CONCLUSIONS

Much research is devoted to the medical application of computational fluid dynamics. While conventional methods to assess lung function are still unrivaled in their diagnostic value for physicians, it can be predicted that computational fluid dynamics will, in the near future, influence clinical decisions.

In the present work, it has been shown that the use of realistic geometries and boundary conditions is feasible and generates credible results. The SST $k-\omega$ turbulence model, combined with pressure outlets, seems to be the winning combination. If ever this will be applied on a clinical scale, however, some algorithm will need to be provided to perform the iterative process that comes with the pressure outlet boundary condition to get the desired mass fractions.

Since no gold standard is at hand to compare with, we cannot ascertain whether the results obtained are realistic. It would therefore be advisable

to do some experiments in the near future to verify the results, and check whether the methodology used is correct.

Having a realistic geometry is both a blessing and a curse, because while being closer to reality it makes it very difficult to postprocess the lower airways. It would therefore be advisable that more time is spent on the design of the model, ensuring that all outlets are long enough and that grid quality is good. It would also be preferable to generate surfaces, while making the grid, that make it possible to calculate the resistance over the entire airway. Lastly, a hexahedral mesh, if possible, could constitute a further improvement.

Attempts should be made to try and find a better way for visualizing results.

BIBLIOGRAPHY

[1] *Fluent 6.3 Documentation*.

[2] M. Brouns. *Numerical and experimental study of flow and deposition of aerosols in the upper human airways*. PhD thesis, Vrije Universiteit Brussel, 2007.

[3] M. Brouns, S.T. Jayaraju, C. Lacor, J. De Mey, M. Noppen, W. Vincken, and S. Verbanck. Tracheal stenosis: a flow dynamics study. *Journal of Applied Physiology*, 102:1178–1184, 2007.

[4] M. Brouns, S. Verbanck, and C. Lacor. Influence of glottic aperture on the tracheal flow. *Journal of Biomechanics*, 40:165–172, 2007.

[5] Y. A. Cengel and J. Cimbala. *Fluid Mechanics: Fundamentals and Applications*. McGraw-Hill, 2006.

[6] J. De Backer, O.M. Vanderveken, W.G. Vos, A. Devolder, S.L. Verhulst, J.A. Verbraecken, P.M. Parizel, M.J. Braem, P.H. Van de Heyning, and W.A. De Backer. Functional imaging using computational fluid dynamics to predict treatment success of mandibular advancement devices in sleep-disordered breathing. *Journal of Biomechanics*, 40:3708–3714, 2007.

[7] J.W. De Backer, W.G. Vos, A. Devolder, S.L. Verhulst, P. Germonpré, F.L. Wuyts, P.M. Parizel, and W. De Backer. Computational fluid dynamics can detect changes in airway resistance in asthmatics after acute bronchodilation. *Journal of Biomechanics*, 41:106–113, 2008.

[8] J.W. De Backer, W.G. Vos, C.D. Gorlé, P. Germonpré, B. Partoens, F.L. Wuyts, P.M. Parizel, and W. De Backer. Flow analyses in the lower airways: Patient-specific model and boundary conditions. *Medical Engineering & Physics*, 30:872–879, 2008.

[9] J.W. De Backer, W.G. Vos, S.L. Verhulst, and W. De Backer. Novel imaging thechniques using computer methods for the evaluation of the upper airway in patients with sleep-disordered breathing: A comprehensive review. *Sleep Medicine Reviews*, 12:437–447, 2008.

[10] R.K. Freitas and W. Schrder. Numerical investigation of the three-dimensional flow in a human lung flow. *Journal of Biomechanics*, 41:2446–2457, 2008.

[11] T. Gemci, V. Ponyavin, Y. Chen, H. Chen, and R. Collins. Cfd simulation of airflow in a 17-generation digital reference model of the human bronchial tree. *Journal of Biomechanics*, 41:2047–2054, 2008.

[12] A.F. Heenan, E. Matida, A. Pollard, and W.H. Finlay. Experimental measurements and computational modeling of the flow field in an idealized human oropharynx. *Experiments in Fluids*, 35:70–84, 2003.

[13] R.E. Henkin, D. Bova, G.L. Dillehay, S.M. Karesh, J.R. Halama, and R.H. Wagner. *Nuclear Medicine*. Mosby-Elsevier, 2006.

[14] S.T. Jayaraju, M. Brouns, S. Verbanck, and C. Lacor. Fluid flow and particle deposition analysis in a realistic extrathoracic airway model using unstructured grids. *Aerosol Science*, 38:494–508, 2007.

[15] S.T. Jayaraju, M. Brouns, C. Lacor, B. Belkassem, and S. Verbanck. Large eddy and detached eddy simulations of fluid flow and particle deposition in a human mouth-throat. *Aerosol Science*, 39:862–875, 2008.

[16] S.T. Jayaraju, M. Paiva, M. Brouns, C. Lacor, and S. Verbanck. Contribution of upper airway geometry to convective mixing. *Journal of Applied Physiology*, 105:1733–1740, 2008.

[17] C. Lacor. *Computational Fluid Dynamics: Basic Discretisation and Time Stepping Methods*. 2010.

[18] P.W. Longest and S. Vinchurkar. Effects of mesh style and grid convergence on particle deposition in bifurcating airway models with comparisons to experimental data. *Medical Engineering & Physics*, 29:350–366, 2007.

[19] H.Y. Luo and Y. Liu. Modeling the bifurcating flow in a ct-scanned human lung airway. *Journal of Biomechanics*, 41:2681–2688, 2008.

[20] F.R. Menter. Two equation eddy-viscosity turbulence models for engineering applications. *AIAA Journal*, 32-8:1598–1605, 1994.

[21] N. Nowak, P.P. Kakade, and A.V. Annapragada. Computational fluid dynamics simulation of airflow and aerosol deposition in human lungs. *Annals of Biomedical Engineering*, 31:374–390, 2003.

[22] Respiratory System, May 2010. URL http://en.wikipedia.org/wiki/Respiratory_system.

[23] A. Schmidt, S. Zidowitz, A. Kriete, T. Denhard, S. Krass, and H.-O. Peitgen. A digital reference model of the human brochial tree. *Computerized Medical Imaging and Graphics*, 28:203–211, 2004.

[24] W. Vos, J. De Backer, A. Devolder, O. Vanderveken, S. Verhulst, R. Salgado, P. Germonpr, B. Partoens, F. Wuyts, P. Parizel, and W. De Backer. Correlation between severity of sleep apnea and upper airway morphology based on advanced anatomical and functional imaging. *Journal of Biomechanics*, 40:2207–2213, 2007.

[25] W.A. Wall and T. Rabczuk. Fluid-structure interaction in lower airways of ct-based lung geometries. *International Journal for numerical methods in fluids*, 57:653–675, 2008.

[26] E.R. Weibel. Morphology of the human lung. *Academic Press*, 1965.

[27] Z. Zhang, C. Kleinstreuer, and C.S. Kim. Comparison of analytical and cfd models with regard to micron particle deposition in a human 16-generation tracheobronchial airway model. *Aerosol Science*, 40:16–28, 2009.